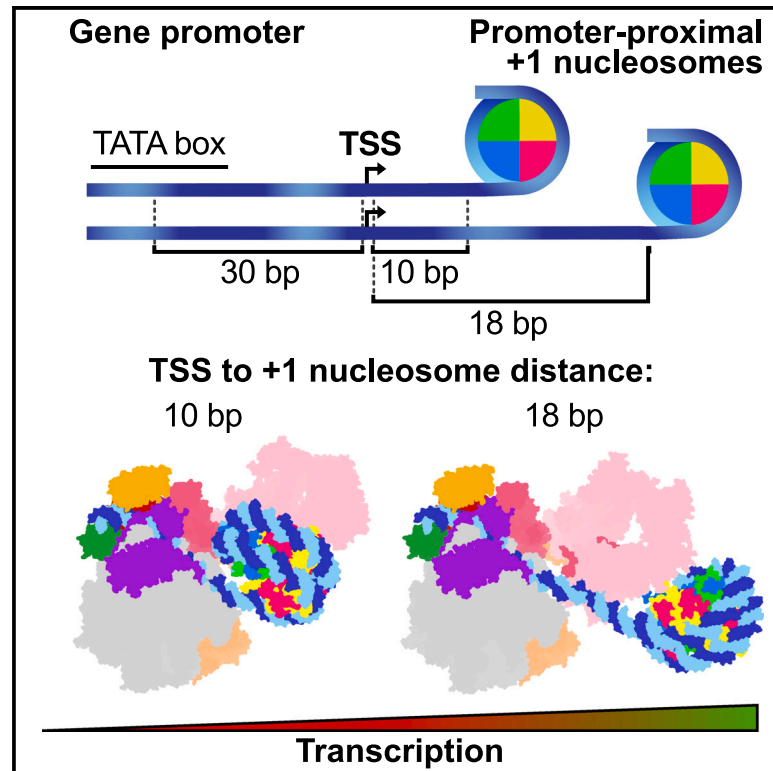


# Structural basis of transcription reduction by a promoter-proximal +1 nucleosome

## Graphical abstract



## Authors

Julio Abril-Garrido,  
Christian Dienemann, Frauke Grabbe,  
Taras Velychko, Michael Lidschreiber,  
Haibo Wang, Patrick Cramer

## Correspondence

haibo.wang@zju.edu.cn (H.W.),  
pcramer@mpinat.mpg.de (P.C.)

## In brief

Through functional assays and cryoelectron microscopy, Abril-Garrido et al. elucidated a mechanism by which the +1 nucleosome reduces transcription. When the +1 nucleosome is located in proximity to the gene promoter, the PIC assembles—albeit in an inhibited state incompatible with DNA opening.

## Highlights

- Promoter proximity of the +1 nucleosome reduces transcription *in vivo* and *in vitro*
- The +1 nucleosome impairs transcription by interfering with productive PIC assembly
- TFIID can bind to the PIC in its closed conformation, but in an inhibited state
- Transcription regulation by the +1 nucleosome depends on its proximity to the TSS



Article

# Structural basis of transcription reduction by a promoter-proximal +1 nucleosome

Julio Abril-Garrido,<sup>1</sup> Christian Dienemann,<sup>1</sup> Frauke Grabbe,<sup>1</sup> Taras Velychko,<sup>1</sup> Michael Lidschreiber,<sup>1</sup> Haibo Wang,<sup>1,2,\*</sup> and Patrick Cramer<sup>1,3,\*</sup>

<sup>1</sup>Max Planck Institute for Multidisciplinary Sciences, Department of Molecular Biology, Am Fassberg 11, 37077 Göttingen, Germany

<sup>2</sup>Present address: Cancer Institute of the Second Affiliated Hospital and Institute of Translational Medicine, Zhejiang University School of Medicine, Hangzhou 310029, China

<sup>3</sup>Lead contact

\*Correspondence: [haibo.wang@zju.edu.cn](mailto:haibo.wang@zju.edu.cn) (H.W.), [pcramer@mpinat.mpg.de](mailto:pcramer@mpinat.mpg.de) (P.C.)

<https://doi.org/10.1016/j.molcel.2023.04.011>

## SUMMARY

At active human genes, the +1 nucleosome is located downstream of the RNA polymerase II (RNA Pol II) pre-initiation complex (PIC). However, at inactive genes, the +1 nucleosome is found further upstream, at a promoter-proximal location. Here, we establish a model system to show that a promoter-proximal +1 nucleosome can reduce RNA synthesis *in vivo* and *in vitro*, and we analyze its structural basis. We find that the PIC assembles normally when the edge of the +1 nucleosome is located 18 base pairs (bp) downstream of the transcription start site (TSS). However, when the nucleosome edge is located further upstream, only 10 bp downstream of the TSS, the PIC adopts an inhibited state. The transcription factor IIH (TFIIH) shows a closed conformation and its subunit XPB contacts DNA with only one of its two ATPase lobes, inconsistent with DNA opening. These results provide a mechanism for nucleosome-dependent regulation of transcription initiation.

## INTRODUCTION

Gene promoters are flanked by nucleosomes that are referred to as −1 and +1 for the first upstream and downstream nucleosome, respectively.<sup>1–6</sup> The +1 nucleosome is located downstream of the transcription start site (TSS), near the RNA polymerase II (RNA Pol II) pre-initiation complex (PIC).<sup>2,3,7–12</sup> The position of the +1 nucleosome varies for genes that are expressed at different levels,<sup>3,13–16</sup> but how the position of a nucleosome influences transcription initiation is not understood. At transcriptionally active mammalian genes, the edge of the +1 nucleosome is located around 40–60 base pairs (bp) downstream of the TSS.<sup>13,17–20</sup> However, at inactive or weakly active genes, the +1 nucleosome is located further upstream, in close proximity to the TSS.<sup>14</sup> This proximal nucleosome position is thought to interfere with PIC formation or function and to regulate gene activity. Reduction of transcription activity by the presence of a proximal nucleosome is consistent with *in vivo* studies in yeast<sup>21–23</sup> and with the long-standing observation that transcription initiation *in vitro* is inhibited by a nucleosome located at the promoter.<sup>7,24–26</sup>

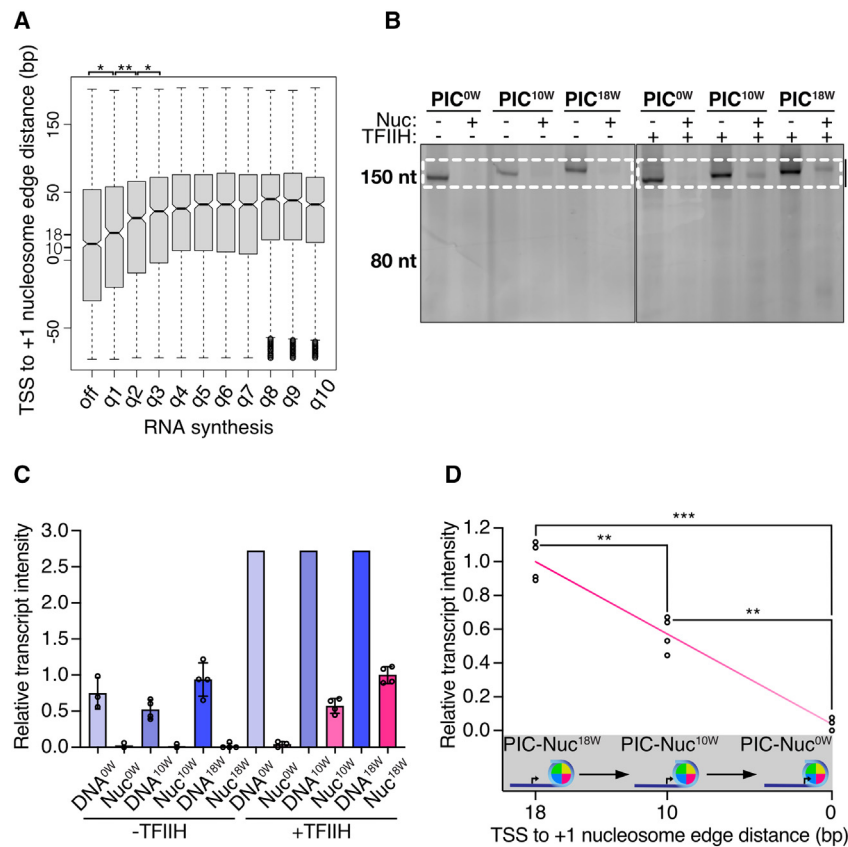
Very recently, the first structural studies of PICs in the presence of a +1 nucleosome were published.<sup>27,28</sup> For human PICs, transcription factor IIH (TFIIH) and Mediator were found to form weak interactions with nucleosomes positioned at distal locations of 40 or 50 bp from the TSS,<sup>27</sup> but proximal nucleosome locations were not investigated. For PICs of the yeast

*Saccharomyces cerevisiae* (*S. cerevisiae*), a high-resolution cryoelectron microscopy (cryo-EM) study found that TFIIH establishes intimate interactions with the nucleosome and that its translocase subunit Ssl2 (XPB in human TFIIH) drives the rotation of the +1 nucleosome, leading to partial detachment of nucleosomal DNA.<sup>28</sup> However, the yeast and human systems differ. In contrast to human RNA Pol II, yeast RNA Pol II does not undergo promoter-proximal pausing and instead scans DNA downstream before initiation.<sup>29–33</sup>

Whereas these published studies provided structural information on PIC-nucleosome interactions, they did not provide insights into how nucleosome positioning regulates transcription.<sup>27,28</sup> It has long been known that compaction of chromatin correlates with a reduction in transcription activity.<sup>34–36</sup> For example, critical biological processes such as heterochromatin maintenance and mitosis have been associated with a reduction in RNA synthesis.<sup>37,38</sup> However, we do not understand the mechanisms by which nucleosomes near the promoter can cause such reduction in gene activity.

Here, we employed a combination of functional and structural studies to investigate the regulatory role of a promoter-proximal +1 nucleosome in mammalian transcription initiation. In particular, we describe how nucleosome proximity to the promoter can regulate transcription using biochemical and cell-based assays and we determine cryo-EM structures of two PIC-nucleosome complexes. We describe that a reduction of RNA synthesis correlates with an upstream shift of





p values for PIC-Nuc<sup>18W</sup>-PIC-Nuc<sup>10W</sup>, PIC-Nuc<sup>18W</sup>-PIC-Nuc<sup>0W</sup>, and PIC-Nuc<sup>10W</sup>-PIC-Nuc<sup>0W</sup> are 4.2E-3, 3.0E-4, and 1.8E-3, respectively (see STAR Methods).

the +1 nucleosome toward the TSS *in vivo*. In addition, we observe that positioning a nucleosome at a TSS-proximal location *in vitro* downregulates transcription by affecting PIC assembly and altering the conformation of TFIIH, which impedes its translocase subunit XPB from fully engaging downstream promoter DNA. Our results suggest that positioning of the +1 nucleosome at a promoter-proximal location can interfere with productive PIC formation and transcription initiation.

## RESULTS

### Promoter proximity of the +1 nucleosome reduces transcription

Various studies have related the proximal location to the TSS of the +1 nucleosome to low gene expression levels,<sup>13,14</sup> but it was thus far not investigated whether genes that contain promoter-proximal nucleosomes indeed show low RNA synthesis rates. To address this, we analyzed transient transcriptome sequencing (TT-seq) and micrococcal nuclease sequencing (MNase-seq) data obtained from HEK293 cells (T. Velychko et al., unpublished data). We split genes into ten groups based on their RNA synthesis levels (inactive and RNA synthesis deciles q1-q10) and calculated the distance from the TSS to the +1 nucleosome edge for genes in each group. We observed that a reduction of RNA synthesis correlates with an upstream shift of

### Figure 1. Promoter proximity of the +1 nucleosome reduces transcription

(A) Boxplots showing TSS to +1 nucleosome edge distances for gene groups with different RNA synthesis levels in HEK293 cells. Genes were split into inactive and deciles of RNA synthesis q1-q10 (low-high, see STAR Methods). Box limits are the first and third quartiles, and the band inside the box is the median. The ends of the whiskers extend the box by 1.5 times the interquartile range. Notches represent 95% confidence intervals for the median values. Statistical significance is denoted above the respective boxplots (\*\*p value < 0.01; \*p value < 0.05). p values for off-q1, q1 and q2, and q2 and q3 are 3.2E-2, 4.0E-3, and 2.6E-2, respectively.

(B) Urea-PAGE of *in vitro* transcription assays where the edge of the nucleosome-positioning sequence is adjacent to the TSS, or 10 and 18 bp downstream of the TSS (PIC<sup>0W</sup>, PIC<sup>10W</sup>, and PIC<sup>18W</sup>, respectively). Transcription reactions were performed with and without TFIIH and the nucleosome. The expected full-length RNA product is indicated with an asterisk. Dashed rectangles denote the area used for quantifications.

(C) Quantifications of the transcription assays shown in (B) (see STAR Methods). Data are represented as mean over replicates (spheres).

(D) TFIIH-dependent transcription of nucleosome-reconstituted DNA templates shows that the proximity of the nucleosome regulates gene activity. Plotted intensities correspond to transcribing PIC complexes in the presence of a nucleosome located at different distances from the TSS. Statistical significance is shown (\*\*p value < 0.001; \*\*p value < 0.01).

the +1 nucleosome (Figure 1A). The median distance from the nucleosome edge to the TSS for moderate-to-highly (q3-q10), weakly (q1 and q2) active, and inactive (off) genes was 44-35, 30-20, and 12 bp, respectively. This suggests that gene activity is reduced when the nucleosome is proximally located to the promoter region *in vivo*.

To corroborate these findings, we carried out *in vitro* transcription assays with highly purified, recombinant human initiation factors and endogenous *Sus scrofa* RNA Pol II, which is 99.9% identical to human RNA Pol II (Figure S1A). For these assays, we used DNA templates containing a +1 nucleosome positioned at increasing distances from the TSS (Figures 1B-1D and 2A). Promoter-dependent *de novo* transcription of nucleosome-containing DNA templates required TFIIH, providing a positive control (Figures 1B and 1C). We found that transcription was reduced ~2.5-fold or ~4.5-fold when templates were used that contained a nucleosome with its edge located either 18 or 10 bp from the TSS (PIC-Nuc<sup>18W</sup> and PIC-Nuc<sup>10W</sup> templates, respectively), when compared with the corresponding nucleosome-free DNA templates (Figure 1C). We further observed that positioning a nucleosome with its edge directly at the TSS (PIC-Nuc<sup>0W</sup>) fully inhibited transcription (Figure 1D), consistent with previous studies.<sup>7,24-26</sup> In summary, shifting a +1 nucleosome from a downstream location to a more promoter-proximal position closer to the TSS reduces transcription activity *in vitro* and *in vivo*.

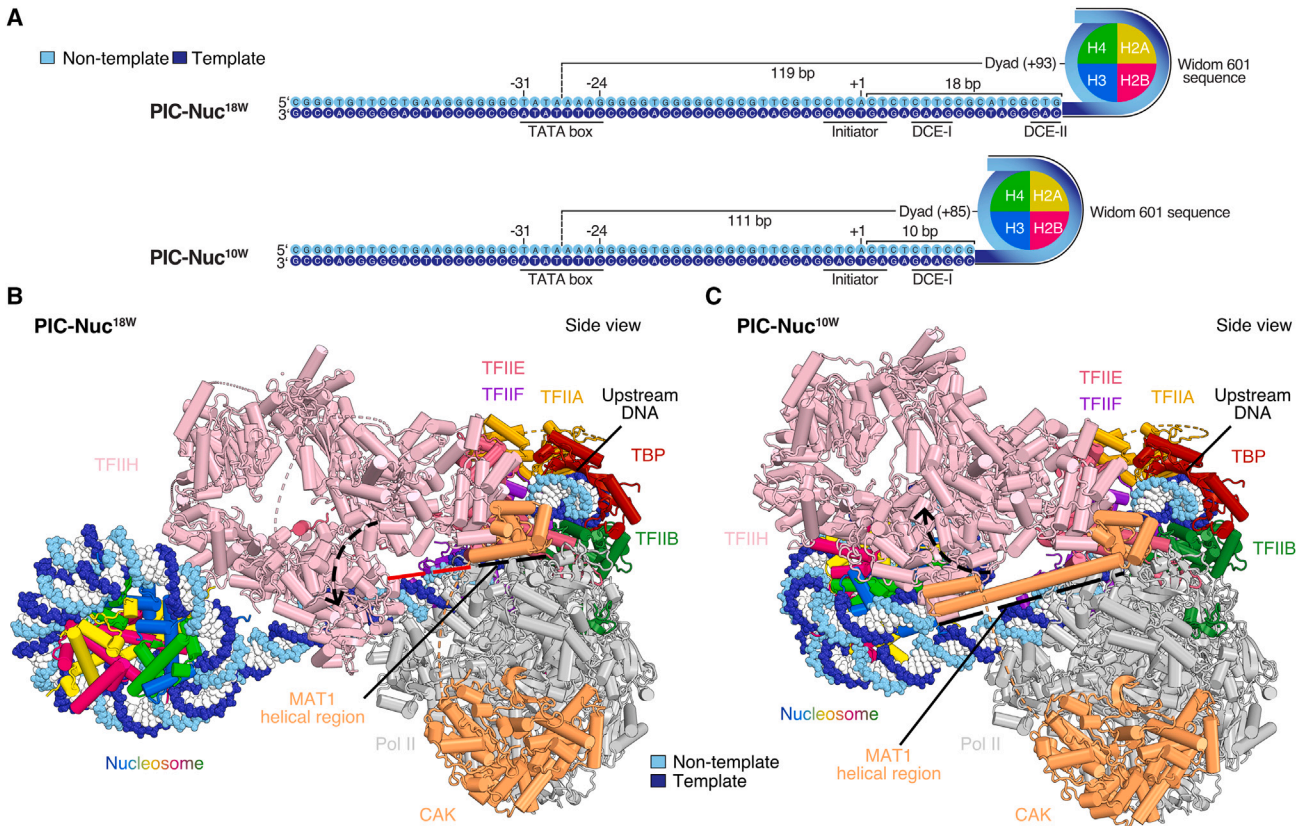


**Figure 2. Structures of PIC-nucleosome complexes**

(A) Scheme of the nucleosome-containing DNA templates used for the structures shown in (B) and (C). Distances between the TSS and the edge of the nucleosome as well as from the TATA-box midpoint to the nucleosome dyad are indicated. Core promoter motifs and the nucleosome-positioning sequences are highlighted with solid lines and curves, respectively.

(B) Model of the mammalian PIC-nucleosome<sup>18W</sup> complex (PIC-Nuc<sup>18W</sup>) shown as cartoon-sphere in side view.

(C) Model of the mammalian PIC-nucleosome<sup>10W</sup> complex (PIC-Nuc<sup>10W</sup>) shown as cartoon-sphere in side view. Major conformational changes between PIC-Nuc<sup>18W</sup> and PIC-Nuc<sup>10W</sup> are indicated with arrowheads. The MAT1 helical region is highlighted with a dashed line (black color denotes ordered and red disordered).

### Mammalian PIC-nucleosome structure

To investigate how the position of the +1 nucleosome influences transcription initiation, we performed cryo-EM analyses of reconstituted PIC-nucleosome complexes. We first designed a DNA promoter containing the edge of the +1 nucleosome 18 bp downstream of the TSS (Figure 2A). This design is consistent with TSS-nucleosome distances we and others found *in vivo* for weakly expressed genes (Figure 1A).<sup>13,14</sup> We reconstituted the PIC on this nucleosome template and determined the structure by cryo-EM analysis at an overall resolution of 4.0 Å (PIC-Nuc<sup>18W</sup>) (Figures 2A, 2B, and S1A–S1D). Signal subtraction and focused refinement strategies improved the resolution of the XPB-containing part of TFIIF, the XPD-containing part of TFIIF, the TFIIF subcomplex CDK-activating kinase module (CAK), the core PIC (cPIC), and the nucleosome to 3.9, 4.7, 3.3, 3.0, and 3.6 Å, respectively (Figures S1D and S2).

In the resulting structure, we observed the canonical conformation of the PIC,<sup>39,40</sup> and only minor movements in the upstream complex containing TBP, TFIIA, and TFIIIB (Figures 2B and S3A), consistent with its previously reported flexibility.<sup>40</sup>

TFIIH adopts an open conformation, as observed in all previous PIC structures (Figures 3A and S3A),<sup>27,39–44</sup> allowing for the complete engagement of both ATPase lobes with DNA (Figure 4A). This is facilitated by the distal position of the nucleosome, which renders the downstream DNA-binding region of XPB nucleosome-free (Figure S3B). This downstream region is slightly bent when compared with the structure of the PIC on a nucleosome-free DNA (Figure S3A).<sup>40</sup> In this PIC-nucleosome structure, about two turns of nucleosomal DNA are detached from the histone octamer at superhelical location (SHL) –5 to SHL –7 (Figure 4B).

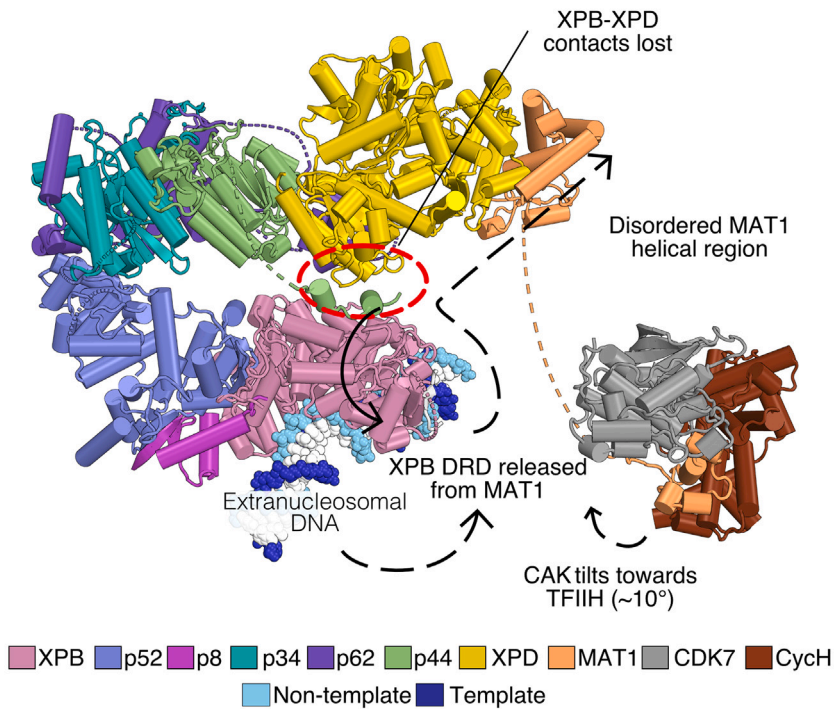
### Nucleosome proximity alters PIC conformation

To investigate the structural basis of transcription reduction by a promoter-proximal +1 nucleosome, we also determined the structure of a PIC-nucleosome complex where the +1 nucleosome was positioned at a more proximal location, with the edge of the nucleosome located 10 bp downstream of the TSS (PIC-Nuc<sup>10W</sup>) (Figures 2A and 2C). We obtained an overall resolution of 4.1 Å for this complex (Figures S4A–S4D). With the



A

**PIC-Nuc<sup>18W</sup>-bound TFIIH (open conformation)**



B

**PIC-Nuc<sup>10W</sup>-bound TFIIH (closed conformation)**

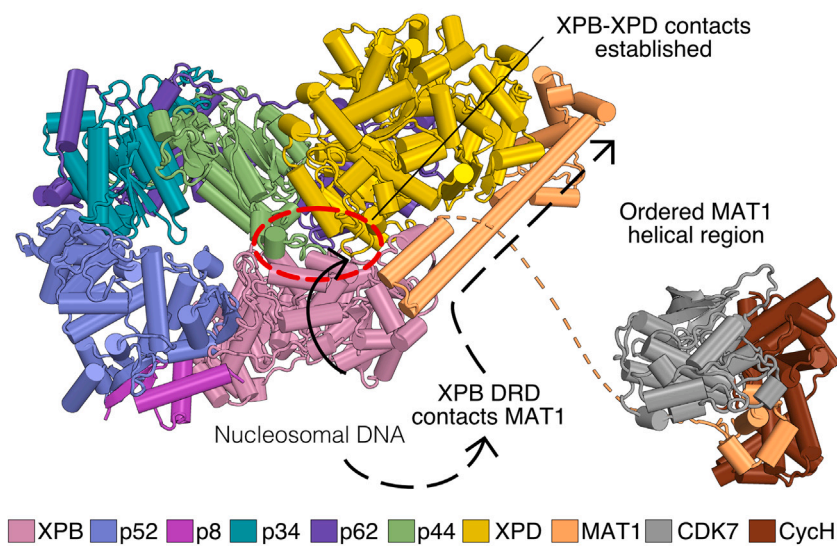


**Figure 3. Nucleosome proximity alters TFIIH conformation**

(A) A distal nucleosome (PIC-Nuc<sup>18W</sup>) induces an open state of TFIIH. Solid and dashed arrowheads denote rearrangements from the closed state, the red dashed oval indicates the region of XPB-XPD contacts.

(B) A proximal nucleosome (PIC-Nuc<sup>10W</sup>) induces a closed state of TFIIH. Solid and dashed arrowheads denote rearrangements from the open state, the red dashed oval indicates the region of XPB-XPD contacts.

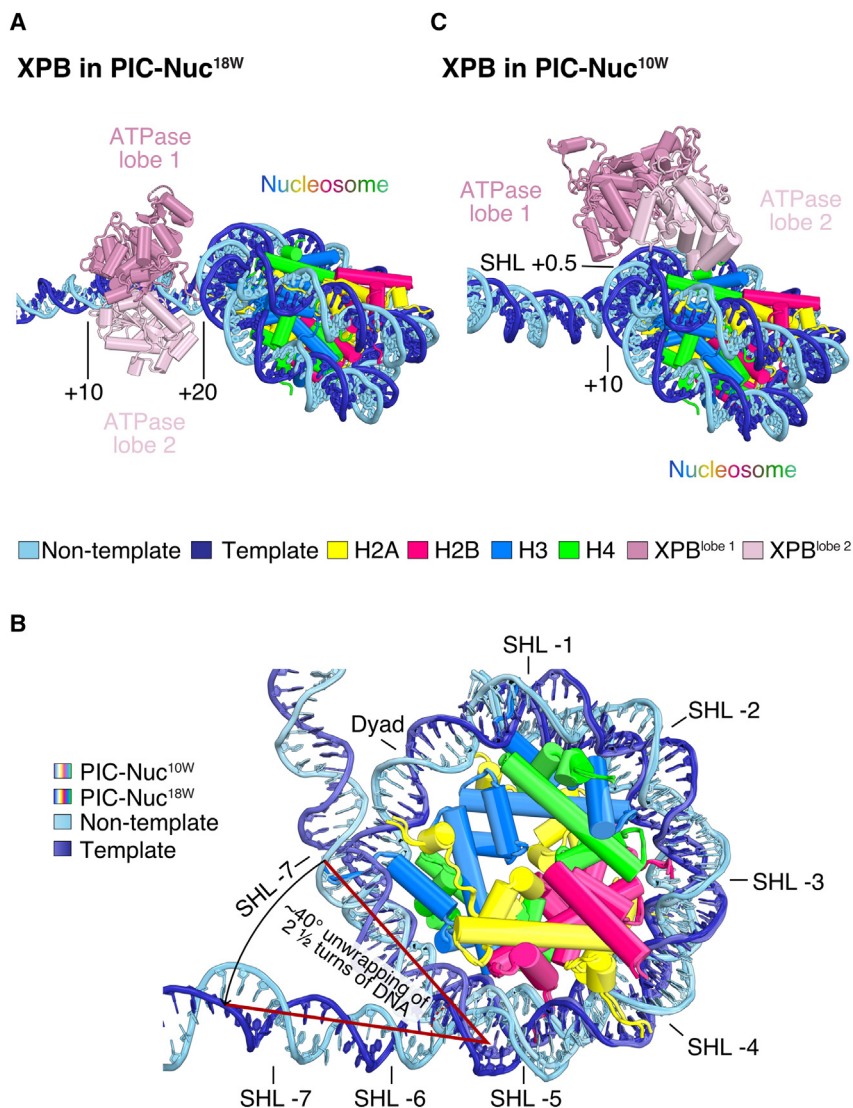


**Figure 4. Nucleosome position alters PIC-DNA contacts**

(A and C) Comparison of XPB binding to (A) a distal (PIC-Nuc<sup>18W</sup>) and (C) proximal nucleosome (PIC-Nuc<sup>10W</sup>) by superimposition on XPB and the nucleosome. The position of the nucleosome alters the DNA binding of the ATPase lobes of the TFIIE subunit XPB. The color code is provided at the bottom legend. Numbers on DNA denote the distance from the TSS.

(B) Cartoon representation of the different nucleosomes determined (PIC-bound), showing distinct nucleosomal DNA wrapping states. Top-left legend specifies the color used for the models. Model superimposition was carried out by aligning on the nucleosome. SHL, superhelical location.

### Closed state of TFIIE is incompatible with DNA opening

In the observed closed state of TFIIE, the XPB translocase subunit, which is essential for opening DNA, cannot fully engage the promoter. Instead, the ATPase lobe 1 binds nucleosomal DNA approximately 88 bp downstream of the TSS, at SHL +0.5, whereas lobe 2 is located ~30 Å away from the DNA (Figure 4C). The observed PIC conformation and PIC-DNA contacts are thus incompatible with promoter DNA opening and transcription initiation. The closed TFIIE conformation was induced by the proximal location of the nucleosome because it is the only difference in the two structure determination experiments. We animated the conformational transition from the closed to the open TFIIE state in Video S1.

During 3D classifications, we could also resolve the cPIC-nucleosome complex lacking TFIIE and TFIIE (cPIC-Nuc<sup>10W</sup>)

use of signal subtraction and focused refinement, we improved the resolution of the reconstructions for the cPIC to 3.1–3.2 Å, for TFIIE to 4.5 Å, for the nucleosome to 3.2–3.5 Å and for the CAK to 3.8 Å (Figures S4D and S5).

In the obtained structure, the conformation of the cPIC (lacking TFIIE) does not deviate from that observed in the PIC-Nuc<sup>18W</sup> structure and is also similar to that observed in the absence of a nucleosome (Figure S6A).<sup>40</sup> However, in contrast to all known PIC structures, TFIIE adopts a closed conformation that had only been observed previously for free TFIIE (Figures 3B and S6B).<sup>39–46</sup> In this closed conformation, the two ATPase subunits, XPB and XPD, contact each other. The TFIIE subunit MAT1 favors this arrangement by contacting the XPB damage recognition domain (DRD) and its helical region stabilizes the closed TFIIE conformation. In summary, these observations show that the more TSS-proximal location of the +1 nucleosome led to an alternative PIC conformation with a closed state of TFIIE.

and refined its structure at 3.8 Å resolution (Figures 5A, S4D, and S5). In this structure, the nucleosome overlaps with the location of TFIIE in a PIC complex as it is shifted by ~20 Å and tilted by ~25°, compared with the complete PIC-Nuc<sup>10W</sup> structure (Figure 5B; Video S2). This is consistent with a proximally positioned +1 nucleosome interfering with complete promoter DNA engagement by TFIIE. We, therefore, suggest that the PIC with the closed TFIIE conformation represents an inhibited state.

### Altered TFIIE-nucleosome contacts

TFIIE bridges the cPIC to the +1 nucleosome in both structures we determined. The comparison of these two structures shows that the rotational position of the nucleosome with respect to TFIIE changes (Figures 2B and 2C). As a consequence, TFIIE engages differently with promoter DNA, and its contacts with the nucleosome are altered. In the PIC-Nuc<sup>18W</sup> structure (Figure 6A), the TFIIE subunit p52 establishes most of the nucleosome

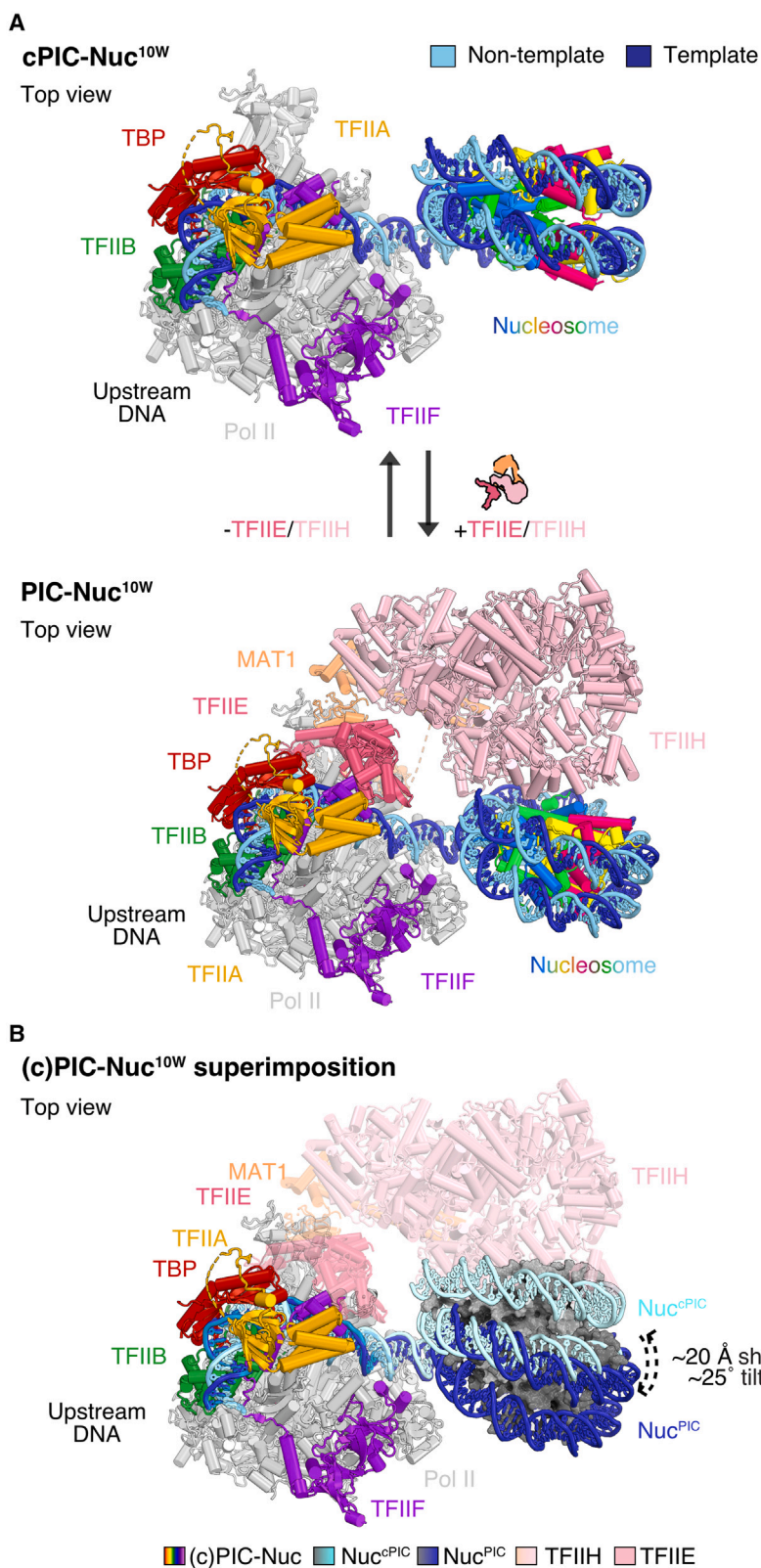


**Figure 5. Structural transition of the nucleosome upon binding or release of TFIIE and TFIIH on the cPIC-Nuc<sup>10W</sup>**

(A) Top views of the cPIC-Nuc<sup>10W</sup> (lacking TFIIE and TFIIH, top panel) and PIC-Nuc<sup>10W</sup> (bottom panel).

(B) Overlay of both structural models shown in (A), showing a conformational change of the nucleosome depending on the presence of TFIIE and TFIIH. Arrowheads describe the direction of such movements. Superimposition of the models was performed by aligning on RNA Pol II. Histone octamers are depicted in different shades of the gray surface. Colors of different protein subunits or DNA strands are depicted in the figure or at the bottom legend.



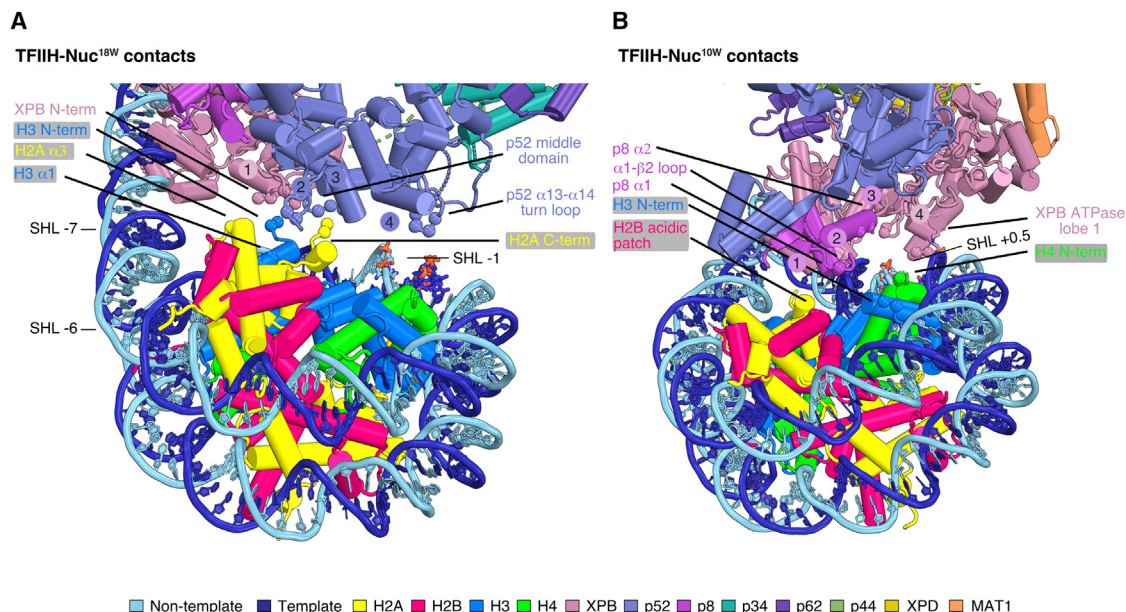


**Figure 6. TFIIF-nucleosome contacts**

(A) Cartoon representation showing interactions between TFIIF and the nucleosome in PIC-Nuc<sup>18W</sup>. Residues T51, K52, D54, and Q64 of the XPB N terminus (interface 1) interact mainly electrostatically with the N-terminal tail (NTT) of H3 (residues 37–41). p52 acidic residues (E189, E192, interface 2) contact basic residues from both H2A  $\alpha$ 3 (K74) and H3  $\alpha$ 1 (R52, K56), and its residues 168–170 (interface 3) establish backbone interactions with residues 118–119 of H2A C terminus. In addition, mostly basic residues of the p52  $\alpha$ 13– $\alpha$ 14 loop (274–278, interface 4) bind to the minor groove adjacent to the nucleosome dyad (SHL –1). SHL, superhelical location.

(B) Cartoon representation showing interactions between TFIIF and the nucleosome in PIC-Nuc<sup>10W</sup>. Residues K31–N27 (interface 1), R56 (interface 2), and Q63 (interface 3) of the p8 subunit make electrostatic contacts to the H2B acidic patch, and the N-terminal regions of H3 (D81) and H4 (R23), respectively. XPB ATPase lobe 1 residues 416–420 and K449 (interface 4) engulf the DNA major groove adjacent to the nucleosome dyad (SHL +0.5). SHL, superhelical location. The positions of the C- $\alpha$  atoms of interacting residues are shown as spheres.

contacts, with mostly basic residues within the  $\alpha$ 13– $\alpha$ 14 loop (residues 274–278) binding nucleosomal DNA at SHL –1, and acidic residues of the p52 middle domain interacting with basic amino acids of the C terminus of H2A and H3  $\alpha$ 1. The N-terminal region of XPB contacts the N-terminal region of histone H3. Conversely, in the PIC-Nuc<sup>10W</sup> structure (Figure 6B), the p8 subunit contacts the H2B acidic patch of the nucleosome and the N-terminal regions of H3 and H4. Basic residues of XPB ATPase lobe 1 bind to nucleosomal DNA at SHL +0.5, forming a major TFIIF-nucleosome interface.

### TFIIF kinase module and RPB6 NTT

We also observed the TFIIF kinase module (CAK) in our structures (Figures 3 and S7A). The CAK interacts with MED6 and the hook of Mediator in previously determined Mediator-PIC complexes, positioning CAK far from the RNA Pol II surface.<sup>41,42,44</sup> In our structures, however, the CAK docks between the RPB1 foot and the RNA Pol II stalk (RPB4–RPB7), using its subunit cyclin H (CycH) to form a wedge between them. The N-terminal region of the CAK CycH subunit contacts the RPB1 linker helix connecting to the C-terminal domain (CTD) and the RPB7  $\alpha$ 1– $\alpha$ 2 loop, whereas the C-terminal helix of CycH mostly establishes charge-based interactions with the RPB1 foot helix  $\alpha$ 28 and  $\alpha$ 31 (Figure S7B). This location had been previously observed with different levels of confidence in yeast<sup>47</sup> and humans (Figure S7C).<sup>43,48</sup>

Finally, in our structures, we observed an extra density in the RNA Pol II cleft (Figure S7D). Based on the similar location found for the yeast N-terminal tail (NTT) of the RNA Pol II subunit Rpb6,<sup>28</sup> we suggest that this density is due to the mammalian counterpart in RPB6 (Figures S7E and S7F). Whereas the *S. cerevisiae* NTT is located over the RNA Pol II bridge helix, the density of the putative mammalian NTT locates closer to RPB1 helix  $\alpha$ 37 (Figure S7F). Consistent with findings in yeast,<sup>28</sup> the cryo-EM density shows clashes between the putative NTT and a modeled DNA template in the active center (Figure S7G), indicating that the NTT must be released from the cleft upon formation of an open complex.

### DISCUSSION

Here, we combine structural and functional studies to show that a promoter-proximal +1 nucleosome can reduce transcription activity and provide a mechanism for such +1 nucleosome-dependent gene regulation (Figure 7). When the nucleosome is located with its edge  $\sim$ 2 turns of DNA downstream of the TSS, the PIC assembles normally and TFIIF adopts an open conformation that is fully engaged with promoter DNA, as required for DNA opening. However, when the nucleosome is positioned with its edge only  $\sim$ 1 turn of DNA downstream of the TSS, TFIIF adopts a closed conformation and can only partially engage with DNA, consistent with a reduction in transcription activity.



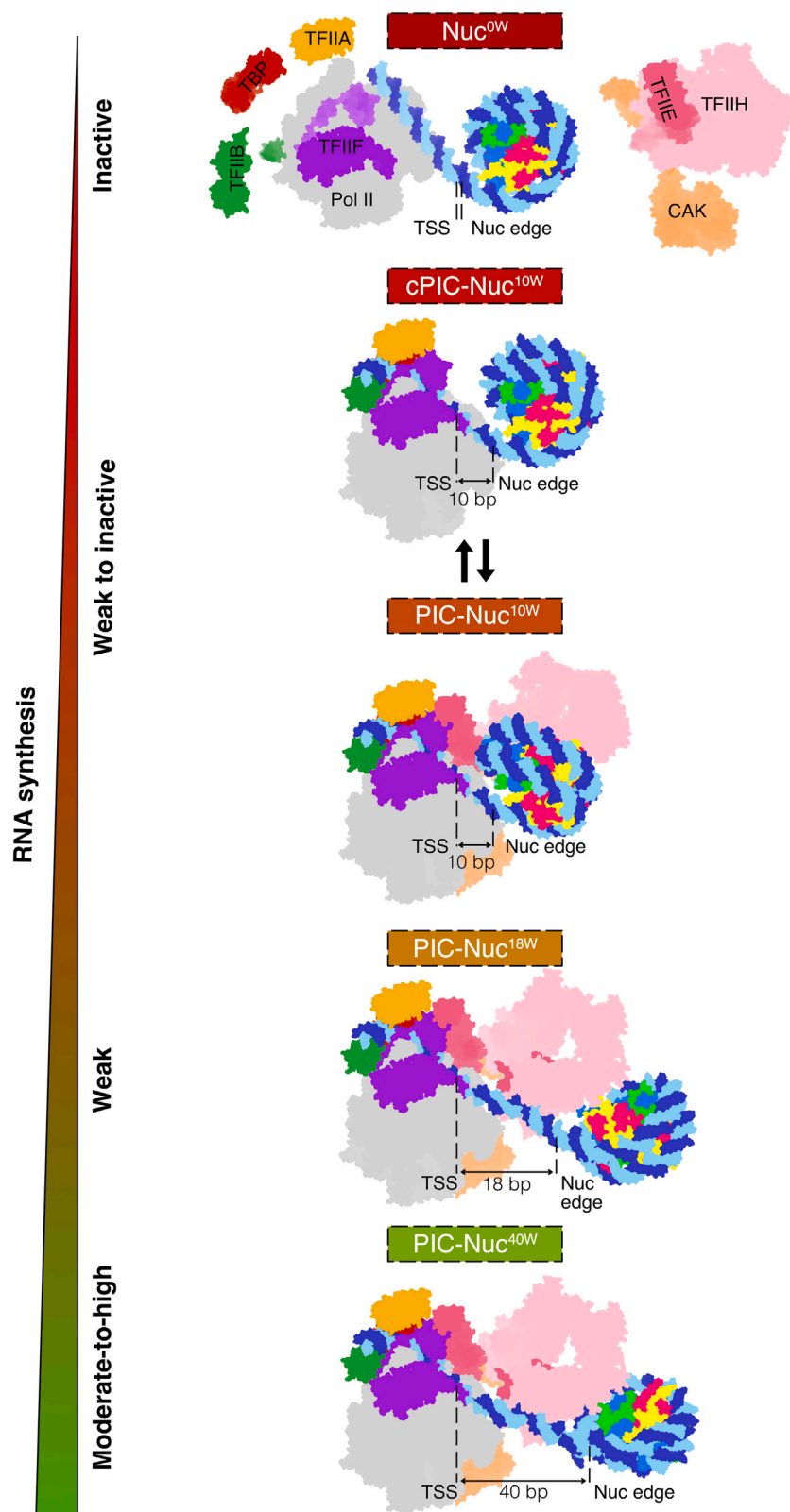


**Figure 7. Model of transcription reduction by a +1 nucleosome**

The proximity of a downstream nucleosome to the promoter region of a gene distinctly reduces RNA Pol II-mediated RNA synthesis by changing the binding of TFIIF to promoter DNA. The model of PIC-Nuc<sup>40W</sup> belongs to PDB: 8GXS.<sup>27</sup> Different gene categories and a gradient showing decreasing RNA synthesis are denoted on the left (green, high synthesis; red, no synthesis).

When the closed conformation of TFIIH was first observed, it was thought to be a feature that is specific to the PIC-unbound, free TFIIH complex.<sup>45,46</sup> However, our results show that TFIIH can adopt its closed conformation also within the PIC, where it may serve to regulate TFIIH activity. Superposition of our PIC-nucleosome structures onto a cPIC structure with open promoter DNA,<sup>40</sup> shows that, upon TFIIH-independent DNA opening, the nucleosome would sterically clash with the RNA Pol II clamp and the TFIIE winged helix domain (Figure S8), providing a possible explanation for the requirement of TFIIH for transcription of nucleosomal templates. Overall, this suggests that a promoter-proximal nucleosome can have an inhibitory role in transcription initiation by interfering with productive PIC formation, altering DNA binding of TFIIH and its conformation, thus impairing promoter DNA opening and subsequent RNA synthesis.

Structural work on Mediator-PIC complexes revealed that the presence of Mediator positions the TFIIH kinase module (CAK) in close vicinity of its hook region and MED6 subunit,<sup>41,42,44</sup> suggesting Mediator is a key player in relocating the CAK module to make accessible the RNA Pol II CTD for CDK7-mediated phosphorylation. On the contrary, in our structures, we observe the CAK located between the RPB1 foot and the RNA Pol II stalk (RPB4–RPB7), without evidence for the presence of the RNA Pol II CTD. This alternative location of the CAK had been previously observed, albeit at a low level of confidence (~15 Å resolution), in yeast,<sup>47</sup> proposed in a molecular dynamics study for the human TFIID-free PIC,<sup>48</sup> and recently determined in the presence of TFIID in a PIC.<sup>43</sup> Here, we therefore provide evidence that the position of the kinase is conserved from yeast to human and confirm that it is TFIID-independent and Mediator-dependent.

Comparison of our structures with the recently published yeast PIC-nucleosome complex<sup>28</sup> shows that even in our productive PIC structure (PIC-Nuc<sup>18W</sup>), the nucleosome locates closer to the PIC and TFIIH (Figure S9). Whereas ~2 turns of DNA are detached from the histone octamer in our PIC-Nuc<sup>18W</sup> structure, only ~1 turn of DNA is detached in the previous yeast structure.<sup>28</sup> We suggest that the different rotational positions of the nucleosome in these structures lead to different degrees of nucleosomal DNA detachment, consistent with the observation that the parts of TFIIH contacting the nucleosome are not highly conserved.<sup>49</sup> Consequently, whereas nucleosome contacts are formed by p52 in our PIC-Nuc<sup>18W</sup> structure, they are formed by the p52-p8 dimerization domain in the yeast structure.

Finally, our work complements recently published human PIC-nucleosome structures that used much larger TSS-nucleosome distances that are found at active genes (Figure S9).<sup>27</sup> In the published work, the PIC adopts the canonical conformation, where TFIIH and Mediator form contacts with the nucleosome that are suggested to enhance transcription.<sup>27</sup> By contrast, we show that shifting the +1 nucleosome to a TSS-proximal location, representative of inactive genes, leads to alternative TFIIH-nucleosome contacts, induces a closed TFIIH conformation and reduces transcription activity. Thus, these studies are complementary and it emerges that the +1 nucleosome can regulate transcription in various ways, dependent on its relative location to the TSS and the PIC.

### Limitations of the study

Cryo-EM data processing aimed at obtaining intermediates at the highest possible resolution, and low-resolution conformational states may have been filtered out during processing. The lack of Mediator or TFIID in our studies does not alter our conclusions, but future work should aim at including such coactivators. The nucleosome has a certain degree of flexibility, and using a strong positioning sequence helps in obtaining stable intermediate complexes that are attainable to cryo-EM structural studies.

### STAR★METHODS

Detailed methods are provided in the online version of this paper and include the following:

- KEY RESOURCES TABLE
- RESOURCE AVAILABILITY
  - Lead contact
  - Materials availability
  - Data and code availability
- METHOD DETAILS
  - Nucleosome reconstitution
  - Assembly of mammalian PIC-nucleosome complexes
  - Cryo-electron microscopy
  - Data processing
  - Model building and refinement
  - *In vitro* transcription assay
  - TT-seq and MNase-seq data analysis
- QUANTIFICATION AND STATISTICAL ANALYSIS

### SUPPLEMENTAL INFORMATION

Supplemental information can be found online at <https://doi.org/10.1016/j.molcel.2023.04.011>.

### ACKNOWLEDGMENTS

We thank U. Steuerwald for maintaining the cryo-EM infrastructure; U. Neef and P. Rus for maintenance of the insect cell culture facility; M. Klein for maintenance of the computing infrastructure; E. Mohammad for pre-processing TT-seq, RNA-seq, and MNase-seq data; E. Oberbeckmann for critically reading the manuscript; and S. Schilbach, S. Aibara, J. Walshe, I. Fianu, and Y. Zhan for discussions. P.C. was supported by the ERC Advanced Investigator Grant CHROMATRANS (grant agreement no. 882357).

### AUTHOR CONTRIBUTIONS

J.A.-G. carried out all experiments and data analysis unless stated otherwise. J.A.-G. and C.D. collected cryo-EM data. J.A.-G. purified RNA Pol II, histones, and prepared nucleosomes, and F.G. assisted with the protein purification of initiation factors. T.V. collected and M.L. analyzed TT-seq, RNA-seq, and MNase-seq data. H.W. and P.C. supervised research. J.A.-G., H.W., and P.C. interpreted the data and wrote the manuscript with input from all authors.

### DECLARATION OF INTERESTS

The authors declare no competing interests.

Received: January 31, 2023

Revised: March 16, 2023

Accepted: April 11, 2023

Published: May 5, 2023

REFERENCES

- Hughes, A.L., and Rando, O.J. (2014). Mechanisms underlying nucleosome positioning in vivo. *Annu. Rev. Biophys.* 43, 41–63. <https://doi.org/10.1146/annurev-biophys-051013-023114>.
- Jiang, C., and Pugh, B.F. (2009). Nucleosome positioning and gene regulation: advances through genomics. *Nat. Rev. Genet.* 10, 161–172. <https://doi.org/10.1038/nrg2522>.
- Serizay, J., Dong, Y., Jänes, J., Chesney, M., Cerrato, C., and Ahringer, J. (2020). Distinctive regulatory architectures of germline-active and somatic genes in *C. elegans*. *Genome Res.* 30, 1752–1765. <https://doi.org/10.1101/gr.265934.120>.
- Kornberg, R.D., and Lorch, Y. (2020). Primary role of the nucleosome. *Mol. Cell* 79, 371–375. <https://doi.org/10.1016/j.molcel.2020.07.020>.
- Lai, W.K.M., and Pugh, B.F. (2017). Understanding nucleosome dynamics and their links to gene expression and DNA replication. *Nat. Rev. Mol. Cell Biol.* 18, 548–562. <https://doi.org/10.1038/nrm.2017.47>.
- Struhl, K., and Segal, E. (2013). Determinants of nucleosome positioning. *Nat. Struct. Mol. Biol.* 20, 267–273. <https://doi.org/10.1038/nsmb.2506>.
- Li, G., Margueron, R., Hu, G., Stokes, D., Wang, Y.H., and Reinberg, D. (2010). Highly compacted chromatin formed in vitro reflects the dynamics of transcription activation in vivo. *Mol. Cell* 38, 41–53. <https://doi.org/10.1016/j.molcel.2010.01.042>.
- Santana, J.F., Collins, G.S., Parida, M., Luse, D.S., and Price, D.H. (2022). Differential dependencies of human RNA polymerase II promoters on TBP, TAF1, TFIIB and XPB. *Nucleic Acids Res.* 50, 9127–9148. <https://doi.org/10.1093/nar/gkac678>.
- Shao, W., and Zeitlinger, J. (2017). Paused RNA polymerase II inhibits new transcriptional initiation. *Nat. Genet.* 49, 1045–1051. <https://doi.org/10.1038/ng.3867>.
- Tramantano, M., Sun, L., Au, C., Labuz, D., Liu, Z., Chou, M., Shen, C., and Luk, E. (2016). Constitutive turnover of histone H2A.Z at yeast promoters requires the preinitiation complex. *eLife* 5. <https://doi.org/10.7554/eLife.14243>.
- Rhee, H.S., and Pugh, B.F. (2012). Genome-wide structure and organization of eukaryotic pre-initiation complexes. *Nature* 483, 295–301. <https://doi.org/10.1038/nature10799>.
- Rossi, M.J., Kuntala, P.K., Lai, W.K.M., Yamada, N., Badjatia, N., Mittal, C., Kuzu, G., Bocklund, K., Farrell, N.P., Blanda, T.R., et al. (2021). A high-resolution protein architecture of the budding yeast genome. *Nature* 592, 309–314. <https://doi.org/10.1038/s41586-021-03314-8>.
- Schones, D.E., Cui, K., Cuddapah, S., Roh, T.Y., Barski, A., Wang, Z., Wei, G., and Zhao, K. (2008). Dynamic regulation of nucleosome positioning in the human genome. *Cell* 132, 887–898. <https://doi.org/10.1016/j.cell.2008.02.022>.
- Valouev, A., Johnson, S.M., Boyd, S.D., Smith, C.L., Fire, A.Z., and Sidow, A. (2011). Determinants of nucleosome organization in primary human cells. *Nature* 474, 516–520. <https://doi.org/10.1038/nature10002>.
- Schwartz, U., Németh, A., Diermeier, S., Exler, J.H., Hansch, S., Maldonado, R., Heizinger, L., Merkl, R., and Längst, G. (2019). Characterizing the nuclease accessibility of DNA in human cells to map higher order structures of chromatin. *Nucleic Acids Res.* 47, 1239–1254. <https://doi.org/10.1093/nar/gky1203>.
- Guenther, M.G., Levine, S.S., Boyer, L.A., Jaenisch, R., and Young, R.A. (2007). A chromatin landmark and transcription initiation at most promoters in human cells. *Cell* 130, 77–88. <https://doi.org/10.1016/j.cell.2007.05.042>.
- Weber, C.M., Ramachandran, S., and Henikoff, S. (2014). Nucleosomes are context-specific, H2A.Z-modulated barriers to RNA polymerase. *Mol. Cell* 53, 819–830. <https://doi.org/10.1016/j.molcel.2014.02.014>.
- Žumer, K., Maier, K.C., Farnung, L., Jaeger, M.G., Rus, P., Winter, G., and Cramer, P. (2021). Two distinct mechanisms of RNA polymerase II elongation stimulation in vivo. *Mol. Cell* 81, 3096–3109.e8. <https://doi.org/10.1016/j.molcel.2021.05.028>.
- Albert, I., Mavrich, T.N., Tomsho, L.P., Qi, J., Zanton, S.J., Schuster, S.C., and Pugh, B.F. (2007). Translational and rotational settings of H2A.Z nucleosomes across the *Saccharomyces cerevisiae* genome. *Nature* 446, 572–576. <https://doi.org/10.1038/nature05632>.
- Mavrich, T.N., Jiang, C., Ioshikhes, I.P., Li, X., Venters, B.J., Zanton, S.J., Tomsho, L.P., Qi, J., Glaser, R.L., Schuster, S.C., et al. (2008). Nucleosome organization in the *Drosophila* genome. *Nature* 453, 358–362. <https://doi.org/10.1038/nature06929>.
- Klein-Brill, A., Joseph-Strauss, D., Appleboim, A., and Friedman, N. (2019). Dynamics of chromatin and transcription during transient depletion of the RSC chromatin remodeling complex. *Cell Rep.* 26, 279–292.e5. <https://doi.org/10.1016/j.celrep.2018.12.020>.
- Kubik, S., Bruzzone, M.J., Challal, D., Dreos, R., Mattarocci, S., Bucher, P., Libri, D., and Shore, D. (2019). Opposing chromatin remodelers control transcription initiation frequency and start site selection. *Nat. Struct. Mol. Biol.* 26, 744–754. <https://doi.org/10.1038/s41594-019-0273-3>.
- Korber, P., and Barbaric, S. (2014). The yeast PHO5 promoter: from single locus to systems biology of a paradigm for gene regulation through chromatin. *Nucleic Acids Res.* 42, 10888–10902. <https://doi.org/10.1093/nar/gku784>.
- Lorch, Y., LaPointe, J.W., and Kornberg, R.D. (1987). Nucleosomes inhibit the initiation of transcription but allow chain elongation with the displacement of histones. *Cell* 49, 203–210. [https://doi.org/10.1016/0092-8674\(87\)90561-7](https://doi.org/10.1016/0092-8674(87)90561-7).
- Knezetic, J.A., and Luse, D.S. (1986). The presence of nucleosomes on a DNA template prevents initiation by RNA polymerase II in vitro. *Cell* 45, 95–104. [https://doi.org/10.1016/0092-8674\(86\)90541-6](https://doi.org/10.1016/0092-8674(86)90541-6).
- Workman, J.L., and Roeder, R.G. (1987). Binding of transcription factor TFIID to the major late promoter during in vitro nucleosome assembly potentiates subsequent initiation by RNA polymerase II. *Cell* 51, 613–622. [https://doi.org/10.1016/0092-8674\(87\)90130-9](https://doi.org/10.1016/0092-8674(87)90130-9).
- Chen, X., Wang, X., Liu, W., Ren, Y., Qu, X., Li, J., Yin, X., and Xu, Y. (2022). Structures of +1 nucleosome-bound PIC-Mediator complex. *Science* 378, 62–68. <https://doi.org/10.1126/science.abn8131>.
- Wang, H., Schilbach, S., Ninov, M., Urlaub, H., and Cramer, P. (2023). Structures of transcription preinitiation complex engaged with the +1 nucleosome. *Nat. Struct. Mol. Biol.* 30, 226–232. <https://doi.org/10.1038/s41594-022-00865-w>.
- Fishburn, J., Galburt, E., and Hahn, S. (2016). Transcription start site scanning and the requirement for ATP during transcription initiation by RNA polymerase II. *J. Biol. Chem.* 291, 13040–13047. <https://doi.org/10.1074/jbc.M116.724583>.
- Qiu, C., Jin, H., Vvedenskaya, I., Llenas, J.A., Zhao, T., Malik, I., Visbisky, A.M., Schwartz, S.L., Cui, P., Cabart, P., et al. (2020). Universal promoter scanning by Pol II during transcription initiation in *Saccharomyces cerevisiae*. *Genome Biol.* 21, 132. <https://doi.org/10.1186/s13059-020-02040-0>.
- Giardina, C., and Lis, J.T. (1993). DNA melting on yeast RNA polymerase II promoters. *Science* 261, 759–762. <https://doi.org/10.1126/science.8342041>.
- Core, L.J., and Lis, J.T. (2008). Transcription regulation through promoter-proximal pausing of RNA polymerase II. *Science* 319, 1791–1792. <https://doi.org/10.1126/science.1150843>.
- Rougvie, A.E., and Lis, J.T. (1988). The RNA polymerase II molecule at the 5' end of the uninduced hsp70 gene of *D. melanogaster* is transcriptionally engaged. *Cell* 54, 795–804. [https://doi.org/10.1016/s0092-8674\(88\)91087-2](https://doi.org/10.1016/s0092-8674(88)91087-2).
- Eberharter, A., and Becker, P.B. (2002). Histone acetylation: a switch between repressive and permissive chromatin. Second in review series on chromatin dynamics. *EMBO Rep.* 3, 224–229. <https://doi.org/10.1093/embo-reports/kvf053>.

35. Kornberg, R.D., and Lorch, Y. (2002). Chromatin and transcription: where do we go from here. *Curr. Opin. Genet. Dev.* *12*, 249–251. [https://doi.org/10.1016/s0959-437x\(02\)00293-9](https://doi.org/10.1016/s0959-437x(02)00293-9).
36. Steger, D.J., and Workman, J.L. (1996). Remodeling chromatin structures for transcription: what happens to the histones? *BioEssays* *18*, 875–884. <https://doi.org/10.1002/bies.950181106>.
37. Palozola, K.C., Donahue, G., Liu, H., Grant, G.R., Becker, J.S., Cote, A., Yu, H., Raj, A., and Zaret, K.S. (2017). Mitotic transcription and waves of gene reactivation during mitotic exit. *Science* *358*, 119–122. <https://doi.org/10.1126/science.aal4671>.
38. Penagos-Puig, A., and Furlan-Magaril, M. (2020). Heterochromatin as an important driver of genome organization. *Front. Cell Dev. Biol.* *8*, 579137. <https://doi.org/10.3389/fcell.2020.579137>.
39. He, Y., Yan, C., Fang, J., Inouye, C., Tjian, R., Ivanov, I., and Nogales, E. (2016). Near-atomic resolution visualization of human transcription promoter opening. *Nature* *533*, 359–365. <https://doi.org/10.1038/nature17970>.
40. Aibara, S., Schilbach, S., and Cramer, P. (2021). Structures of mammalian RNA polymerase II pre-initiation complexes. *Nature* *594*, 124–128. <https://doi.org/10.1038/s41586-021-03554-8>.
41. Abdella, R., Talyzina, A., Chen, S., Inouye, C.J., Tjian, R., and He, Y. (2021). Structure of the human Mediator-bound transcription preinitiation complex. *Science* *372*, 52–56. <https://doi.org/10.1126/science.abg3074>.
42. Rengachari, S., Schilbach, S., Aibara, S., Dienemann, C., and Cramer, P. (2021). Structure of the human Mediator-RNA polymerase II pre-initiation complex. *Nature* *594*, 129–133. <https://doi.org/10.1038/s41586-021-03555-7>.
43. Chen, X., Qi, Y., Wu, Z., Wang, X., Li, J., Zhao, D., Hou, H., Li, Y., Yu, Z., Liu, W., et al. (2021). Structural insights into preinitiation complex assembly on core promoters. *Science* *372*, eaba8490. <https://doi.org/10.1126/science.aba8490>.
44. Chen, X., Yin, X., Li, J., Wu, Z., Qi, Y., Wang, X., Liu, W., and Xu, Y. (2021). Structures of the human Mediator and Mediator-bound preinitiation complex. *Science* *372*, eabg0635. <https://doi.org/10.1126/science.abg0635>.
45. Greber, B.J., Nguyen, T.H.D., Fang, J., Afonine, P.V., Adams, P.D., and Nogales, E. (2017). The cryo-electron microscopy structure of human transcription factor IIH. *Nature* *549*, 414–417. <https://doi.org/10.1038/nature23903>.
46. Greber, B.J., Toso, D.B., Fang, J., and Nogales, E. (2019). The complete structure of the human TFIID core complex. *eLife* *8*, e44771. <https://doi.org/10.7554/eLife.44771>.
47. Tsai, K.L., Yu, X.D., Gopalan, S., Chao, T.C., Zhang, Y., Florens, L., Washburn, M.P., Murakami, K., Conaway, R.C., Conaway, J.W., and Asturias, F.J. (2017). Mediator structure and rearrangements required for holoenzyme formation. *Nature* *544*, 196–201. <https://doi.org/10.1038/nature21393>.
48. Yan, C.L., Dodd, T., He, Y., Tainer, J.A., Tsutakawa, S.E., and Ivanov, I. (2019). Transcription preinitiation complex structure and dynamics provide insight into genetic diseases. *Nat. Struct. Mol. Biol.* *26*, 397–406. <https://doi.org/10.1038/s41594-019-0220-3>.
49. Rimel, J.K., and Taatjes, D.J. (2018). The essential and multifunctional TFIID complex. *Protein Sci.* *27*, 1018–1037. <https://doi.org/10.1002/pro.3424>.
50. Vos, S.M., Farnung, L., Urlaub, H., and Cramer, P. (2018). Structure of paused transcription complex Pol II-DSIF-NELF. *Nature* *560*, 601–606. <https://doi.org/10.1038/s41586-018-0442-2>.
51. Kocic, G., Chernev, A., Tegunov, D., Dienemann, C., Urlaub, H., and Cramer, P. (2019). Structural basis of TFIID activation for nucleotide excision repair. *Nat. Commun.* *10*, 2885. <https://doi.org/10.1038/s41467-019-10745-5>.
52. Dyer, P.N., Edayathumangalam, R.S., White, C.L., Bao, Y., Chakravarthy, S., Muthurajan, U.M., and Luger, K. (2004). Reconstitution of nucleosome core particles from recombinant histones and DNA. *Methods Enzymol.* *375*, 23–44. [https://doi.org/10.1016/s0076-6879\(03\)75002-2](https://doi.org/10.1016/s0076-6879(03)75002-2).
53. Hu, X., Malik, S., Negroui, C.C., Hubbard, K., Velalar, C.N., Hampton, B., Grosu, D., Catalano, J., Roeder, R.G., and Gnat, A. (2006). A Mediator-responsive form of metazoan RNA polymerase II. *Proc. Natl. Acad. Sci. USA* *103*, 9506–9511. <https://doi.org/10.1073/pnas.0603702103>.
54. Mastronarde, D.N. (2005). Automated electron microscope tomography using robust prediction of specimen movements. *J. Struct. Biol.* *152*, 36–51. <https://doi.org/10.1016/j.jsb.2005.07.007>.
55. Punjani, A., Rubinstein, J.L., Fleet, D.J., and Brubaker, M.A. (2017). cryoSPARC: algorithms for rapid unsupervised cryo-EM structure determination. *Nat. Methods* *14*, 290–296. <https://doi.org/10.1038/nmeth.4169>.
56. Scheres, S.H.W. (2020). Amyloid structure determination in RELION-3.1. *Acta Crystallogr. D Struct. Biol.* *76*, 94–101. <https://doi.org/10.1107/S2059798319016577>.
57. Zivanov, J., Nakane, T., Forsberg, B.O., Kimanius, D., Hagen, W.J., Lindahl, E., and Scheres, S.H. (2018). New tools for automated high-resolution cryo-EM structure determination in RELION-3. *eLife* *7*, e42166. <https://doi.org/10.7554/eLife.42166>.
58. Tegunov, D., and Cramer, P. (2019). Real-time cryo-electron microscopy data preprocessing with Warp. *Nat. Methods* *16*, 1146–1152. <https://doi.org/10.1038/s41592-019-0580-y>.
59. Afonine, P.V., Poon, B.K., Read, R.J., Sobolev, O.V., Terwilliger, T.C., Urzhumtsev, A., and Adams, P.D. (2018). Real-space refinement in PHENIX for cryo-EM and crystallography. *Acta Crystallogr. D Struct. Biol.* *74*, 531–544. <https://doi.org/10.1107/S2059798318006551>.
60. Schrödinger, L., and Delano, W. (2020). PyMOL v2.5.0. <http://www.pymol.org/pymol>.
61. Pettersen, E.F., Goddard, T.D., Huang, C.C., Couch, G.S., Greenblatt, D.M., Meng, E.C., and Ferrin, T.E. (2004). UCSF Chimera—a visualization system for exploratory research and analysis. *J. Comput. Chem.* *25*, 1605–1612. <https://doi.org/10.1002/jcc.20084>.
62. Goddard, T.D., Huang, C.C., Meng, E.C., Pettersen, E.F., Couch, G.S., Morris, J.H., and Ferrin, T.E. (2018). UCSF ChimeraX: meeting modern challenges in visualization and analysis. *Protein Sci.* *27*, 14–25. <https://doi.org/10.1002/pro.3235>.
63. Croll, T.I. (2018). ISOLDE: a physically realistic environment for model building into low-resolution electron-density maps. *Acta Crystallogr. D Struct. Biol.* *74*, 519–530. <https://doi.org/10.1107/S2059798318002425>.
64. Emsley, P., Lohkamp, B., Scott, W.G., and Cowtan, K. (2010). Features and development of coot. *Acta Crystallogr. D Biol. Crystallogr.* *66*, 486–501. <https://doi.org/10.1107/S0907444910007493>.
65. Schindelin, J., Arganda-Carreras, I., Frise, E., Kaynig, V., Longair, M., Pietzsch, T., Preibisch, S., Rueden, C., Saalfeld, S., Schmid, B., et al. (2012). Fiji: an open-source platform for biological-image analysis. *Nat. Methods* *9*, 676–682. <https://doi.org/10.1038/nmeth.2019>.
66. Wang, H., Farnung, L., Dienemann, C., and Cramer, P. (2020). Structure of H3K36-methylated nucleosome-PWWP complex reveals multivalent cross-gyre binding. *Nat. Struct. Mol. Biol.* *27*, 8–13. <https://doi.org/10.1038/s41594-019-0345-4>.
67. Boehning, M., Dugast-Darzacq, C., Rankovic, M., Hansen, A.S., Yu, T., Marie-Nelly, H., McSwiggen, D.T., Kocic, G., Dailey, G.M., Cramer, P., et al. (2018). RNA polymerase II clustering through carboxy-terminal domain phase separation. *Nat. Struct. Mol. Biol.* *25*, 833–840. <https://doi.org/10.1038/s41594-018-0112-y>.
68. Bernecky, C., Herzog, F., Baumeister, W., Plietzko, J.M., and Cramer, P. (2016). Structure of transcribing mammalian RNA polymerase II. *Nature* *529*, 551–554. <https://doi.org/10.1038/nature16482>.
69. Plaschka, C., Hantsche, M., Dienemann, C., Burzinski, C., Plietzko, J., and Cramer, P. (2016). Transcription initiation complex structures elucidate DNA opening. *Nature* *533*, 353–358. <https://doi.org/10.1038/nature17990>.
70. Schilbach, S., Hantsche, M., Tegunov, D., Dienemann, C., Wigge, C., Urlaub, H., and Cramer, P. (2017). Structures of transcription pre-initiation complex with TFIID and Mediator. *Nature* *551*, 204–209. <https://doi.org/10.1038/nature24282>.



71. Kastner, B., Fischer, N., Golas, M.M., Sander, B., Dube, P., Boehringer, D., Hartmuth, K., Deckert, J., Hauer, F., Wolf, E., et al. (2008). GraFix: sample preparation for single-particle electron cryomicroscopy. *Nat. Methods* 5, 53–55. <https://doi.org/10.1038/nmeth1139>.
72. Greber, B.J., Perez-Bertoldi, J.M., Lim, K., Iavarone, A.T., Toso, D.B., and Nogales, E. (2020). The cryoelectron microscopy structure of the human CDK-activating kinase. *Proc. Natl. Acad. Sci. USA* 117, 22849–22857. <https://doi.org/10.1073/pnas.2009627117>.
73. Wang, H., Xiong, L., and Cramer, P. (2021). Structures and implications of TBP-nucleosome complexes. *Proc. Natl. Acad. Sci. USA* 118, e2108859118. <https://doi.org/10.1073/pnas.2108859118>.
74. Chen, V.B., Arendall, W.B., 3rd, Headd, J.J., Keedy, D.A., Immormino, R.M., Kapral, G.J., Murray, L.W., Richardson, J.S., and Richardson, D.C. (2010). MolProbity: all-atom structure validation for macromolecular crystallography. *Acta Crystallogr. D Biol. Crystallogr.* 66, 12–21. <https://doi.org/10.1107/S0907444909042073>.

STAR★METHODS

KEY RESOURCES TABLE

REAGENT or RESOURCE	SOURCE	IDENTIFIER
<b>Bacterial and virus strains</b>		
<i>E. coli</i> BL21 CodonPlus (DE3) RIL	Agilent	Cat#230245
<i>E. coli</i> LOBSTR-BL21(DE3)-RIL	Kerafast	Cat# EC1002
<i>E. coli</i> DH10EMBacY	Geneva Biotech	N/A
<i>E. coli</i> XL-1 Blue	Agilent	Cat#200249
<b>Biological samples</b>		
<i>Sus scrofa</i> thymus	Locally sourced	N/A
<b>Chemicals, peptides, and recombinant proteins</b>		
<i>Sus scrofa</i> RNA polymerase II	Vos et al. <sup>50</sup>	N/A
<i>Homo sapiens</i> TBP	Aibara et al. <sup>40</sup>	N/A
<i>Homo sapiens</i> TFIIB	Aibara et al. <sup>40</sup>	N/A
<i>Homo sapiens</i> TFIIA	Aibara et al. <sup>40</sup>	N/A
<i>Homo sapiens</i> TFIIF	Aibara et al. <sup>40</sup>	N/A
<i>Homo sapiens</i> TFIIE	Aibara et al. <sup>40</sup>	N/A
<i>Homo sapiens</i> TFIIFH-core	This study	N/A
<i>Homo sapiens</i> CAK	Kokic et al. <sup>51</sup>	N/A
<i>Xenopus laevis</i> histones H3, H4, H2A, H2B	Dyer et al. <sup>52</sup>	N/A
8WG16 ( $\alpha$ RPB1 CTD) antibody	Hu et al. <sup>53</sup>	RRID: AB_10013665
Glutaraldehyde 25%	EMS	Cat#16200
Poly(vinyl alcohol)	Sigma-Aldrich	Cat#P8136
RNasin Plus Ribonuclease Inhibitor	Promega	Cat#N2611
Proteinase K	New England Biolabs	Cat#P8107S
Invitrogen UltraPure 0.5M EDTA, pH 8.0	Thermo Fisher Scientific	Cat#15575020
SDS 10%	Thermo Fisher Scientific	Cat#AM9822
DNAseI (RNase-free)	New England Biolabs	Cat#M0303S
Invitrogen Ambion Sodium Acetate (3M), pH 5.5	Thermo Fisher Scientific	Cat#AM9740
NTP Set, 100 mM Solution	Thermo Fisher Scientific	Cat#R0481
SYBR™ Gold Nucleic Acid Gel Stain	Thermo Fisher Scientific	Cat#S11494
BSA-Molecular Biology Grade	New England Biolabs	Cat#B9000S
Urea (RNase-free)	Panreac AppliChem	Cat#A1049
2x RNA Loading Dye	New England Biolabs	Cat#B0363S
DL-Dithiothreitol solution, 1M	Sigma-Aldrich	Cat#43816
40% Acrylamide/bis-acrylamide 19:1	Sigma-Aldrich	Cat#A9926
TRIS borate-EDTA buffer solution (10x)	Sigma-Aldrich	Cat#93290
Phusion DNA Polymerase	House sourced	N/A
Phusion® HF Buffer Pack	New England Biolabs	Cat#B0518S
dNTP Set, 100 mM Solutions	Thermo Fisher Scientific	Cat#R0186
DMSO	Sigma-Aldrich	Cat#D8418
<b>Deposited data</b>		
cPIC-nucleosome <sup>10W</sup> cryo-EM globally refined map	This study	EMD: 16335
Core PIC <sup>cPIC-Nuc10W</sup> cryo-EM focused refined map	This study	EMD: 16336
Nucleosome <sup>cPIC-Nuc10W</sup> cryo-EM focused refined map	This study	EMD: 16337
cPIC-nucleosome <sup>10W</sup> cryo-EM composite map	This study	EMD: 16338
cPIC-nucleosome <sup>10W</sup> model	This study	PDB: 8BZ1

(Continued on next page)

Continued

REAGENT or RESOURCE	SOURCE	IDENTIFIER
PIC-nucleosome <sup>10W</sup> cryo-EM globally refined map	This study	EMD: 16331
Core PIC <sup>PIC-Nuc10W</sup> cryo-EM focused refined map	This study	EMD: 16339
Nucleosome <sup>PIC-Nuc10W</sup> cryo-EM focused refined map	This study	EMD: 16340
TFIIH <sup>PIC-Nuc10W</sup> cryo-EM focused refined map	This study	EMD: 16342
CAK <sup>PIC-Nuc10W</sup> cryo-EM focused refined map	This study	EMD: 16341
PIC-nucleosome <sup>10W</sup> cryo-EM composite map	This study	EMD: 16343
PIC-nucleosome <sup>10W</sup> model	This study	PDB: 8BYQ
PIC-nucleosome <sup>18W</sup> cryo-EM globally refined map	This study	EMD: 16274
Core PIC <sup>PIC-Nuc18W</sup> cryo-EM focused refined map	This study	EMD: 16365
Nucleosome <sup>PIC-Nuc18W</sup> cryo-EM focused refined map	This study	EMD: 16366
TFIIH <sup>PIC-Nuc18W</sup> cryo-EM focused refined map	This study	EMD: 16367
XPB-containing TFIIH <sup>PIC-Nuc18W</sup> cryo-EM focused refined map	This study	EMD: 16367, add.
XPD-containing TFIIH <sup>PIC-Nuc18W</sup> cryo-EM focused refined map	This study	EMD: 16367, add.
CAK <sup>PIC-Nuc18W</sup> cryo-EM focused refined map	This study	EMD: 16368
PIC-nucleosome <sup>18W</sup> cryo-EM composite map	This study	EMD: 16369
PIC-nucleosome <sup>18W</sup> model	This study	PDB: 8BVW

Experimental models: cell lines

Sf9 Cells	Thermo Fisher Scientific	Cat#11496015
High Five Cells	Thermo Fisher Scientific	Cat#B85502

Oligonucleotides

<i>Widom 601</i> template: 5' – ATC GGA TGT ATA TAT CTG ACA CGT GCC TGG AGA CTA GGG AGT AAT CCC CTT GGC GGT TAA AAC GCG GGG GAC AGC GCG TAC GTG CGT TTA AGC GGT GCT AGA GCT GTC TAC GAC CAA TTG AGC GGC CTC GGC ACC GGG ATT CTC GAT – 3'	This work	Integrated DNA Technologies
<i>Widom 601</i> non-template 5' – ATC GAG AAT CCC GGT GCC GAG GCC GCT CAA TTG GTC GTA GAC AGC TCT AGC ACC GCT TAA ACG CAC GTA CGC GCT GTC CCC CGC GTT TTA ACC GCC AAG GGG ATT ACT CCC TAG TCT CCA GGC ACG TGT CAG ATA TAT ACA TCC GAT – 3'	This work	Integrated DNA Technologies
<i>AdML0W</i> cloning forward primer 5' – TCG AGG TAC CGG ATC CGA TAT CCG GGT GTT CCT GAA GGG GGG CTA TAA AAG GGG GTG GGG GCG CGT TCG TCC TCA ATC GAG AAT CCC GGT GCC GAG G – 3'	This work	Sigma-Aldrich
<i>AdML10W</i> cloning forward primer 5' – TCG AGG TAC CGG ATC CGA TAT CCG GGT GTT CCT GAA GGG GGG CTA TAA AAG GGG GTG GGG GCG CGT TCG TCC TCA CTC TCT TCC GAT CGA GAA TCC CGG TGC CGA GG – 3'	This work	Sigma-Aldrich
<i>AdML18W</i> cloning forward primer 5' – TCG AGG TAC CGG ATC CGA TAT CCG GGT GTT CCT GAA GGG GGG CTA TAA AAG GGG GTG GGG GCG CGT TCG TCC TCA CTC TCT TCC GCA TCG CTG ATC GAG AAT CCC GGT GCC GAG G – 3'	This work	Sigma-Aldrich
<i>Widom 601</i> cloning reverse primer 5' – CGA AGA TCT GAT ATC ATC GGA TGT ATA TAT CTG ACA CGT GCC TGG AGAC – 3'	This work	Sigma-Aldrich

(Continued on next page)

**Continued**

REAGENT or RESOURCE	SOURCE	IDENTIFIER
AdMLW PCR forward primer 5' – CGG GTG TTC CTG AAG GGG GGC TAT AAA AGG GGG TG – 3'	This work	Sigma-Aldrich
Widom 601 PCR reverse primer 5' – ATC GGA TGT ATA TAT CTG ACA CGT GCC TGG AGA CTA GGG AG – 3'	This work	Sigma-Aldrich
<b>Recombinant DNA</b>		
438A-hTBP	Aibara et al. <sup>40</sup>	N/A
pOPINF-hTFIIB	Aibara et al. <sup>40</sup>	N/A
438A-hTFIIA	Aibara et al. <sup>40</sup>	N/A
pETDuet-1-hTFIIE	Aibara et al. <sup>40</sup>	N/A
pAHS3C-hTFIIF	Aibara et al. <sup>40</sup>	N/A
438C-XPB-p52-p34-p8-p62-p44-XPB (hTFIIH-core)	This study	N/A
438B-CCNH-CDK7-MAT1 (CAK)	Kokic et al. <sup>51</sup>	N/A
pUC119-AdML0W	This study	N/A
pUC119-AdML10W	This study	N/A
pUC119-AdML18W	This study	N/A
<b>Software and algorithms</b>		
SerialEM 4.0	Mastrorade <sup>54</sup>	<a href="https://bio3d.colorado.edu/SerialEM/#Source">https://bio3d.colorado.edu/SerialEM/#Source</a>
cryoSPARC 3.2.0	Punjani et al. <sup>55</sup>	<a href="https://cryosparc.com/">https://cryosparc.com/</a>
RELION 3.1	Scheres <sup>56</sup> and Zivanov et al. <sup>57</sup>	<a href="https://github.com/3dem/relion">https://github.com/3dem/relion</a>
Warp 1.0.9	Tegunov and Cramer <sup>58</sup>	<a href="http://www.warpem.com">http://www.warpem.com</a>
PHENIX 1.19.2	Afonine et al. <sup>59</sup>	<a href="http://www.phenix-online.org">http://www.phenix-online.org</a>
PyMol 2.5.0	Schrodinger and Delano <sup>60</sup>	<a href="http://www.pymol.org">http://www.pymol.org</a>
UCSF Chimera	Pettersen et al. <sup>61</sup>	<a href="https://www.cgl.ucsf.edu/chimera/">https://www.cgl.ucsf.edu/chimera/</a>
UCSF Chimera X-1.4	Goddard et al. <sup>62</sup>	<a href="https://www.cgl.ucsf.edu/chimerax/">https://www.cgl.ucsf.edu/chimerax/</a>
ISOLDE 1.3	Croll <sup>63</sup>	<a href="https://isolde.cimr.cam.ac.uk/">https://isolde.cimr.cam.ac.uk/</a>
Coot 0.9.6	Emsley et al. <sup>64</sup>	<a href="https://www2.mrc-lmb.cam.ac.uk/personal/pemsley/cool/">https://www2.mrc-lmb.cam.ac.uk/personal/pemsley/cool/</a>
ImageJ 2.1.0	Schindelin et al. <sup>65</sup>	<a href="https://imagej.nih.gov/ij/index.html">https://imagej.nih.gov/ij/index.html</a>
Prism 9.1.0	GraphPad Software Inc (California, USA)	<a href="https://www.graphpad.com/">https://www.graphpad.com/</a>
<b>Other</b>		
Glacios	Thermo Fisher Scientific	N/A
Falcon-III Direct Electron Detector	Thermo Fisher Scientific	N/A
Titan Krios G2	FEI/Thermo Fisher Scientific	N/A
QuantumLS energy filter	Gatan	N/A
K3 Summit Direct Electron Detector	Gatan	N/A
Typhoon™ 9500 FLA imager	GE Healthcare Life Sciences	N/A
BioComp Gradient Master 108	BioComp Instruments	N/A
Model 491 Prep Cell	Bio-Rad	Cat#1702927
Slide-A-Lyzer™ MINI Dialysis Devices (3.5 kDa MWCO)	Thermo Fisher Scientific	Cat# 69552
Slide-A-Lyzer™ MINI Dialysis Devices (20 kDa MWCO)	Thermo Fisher Scientific	Cat# 69590
Amicon Millipore 15 ml (50 kDa MWCO)	MERCK Millipore	Cat# UFC9050
Quantifoil™ R3.5/1, copper, mesh 200	Quantifoil	N/A

**RESOURCE AVAILABILITY**

**Lead contact**

Correspondence and requests for materials should be addressed to P.C. ([pcramer@mpinat.mpg.de](mailto:pcramer@mpinat.mpg.de)).



### Materials availability

Materials are available from Patrick Cramer upon request under a material transfer agreement with the Max Planck Society.

### Data and code availability

- Cryo-EM density maps have been deposited in the Electron Microscopy Data Bank (EMDB) and coordinates within the Protein Data Bank (PDB) for cPIC-nucleosome<sup>10W</sup> (accession codes EMDB: EMD-16335 and PDB: 8BZ1, and EMDB: EMD-16336, EMD-16337, and EMD-16338 for focused refinement maps of cPIC, nucleosome, and composite map, respectively), PIC-nucleosome<sup>10W</sup> (accession codes EMDB: EMD-16331 and PDB: 8BYQ, and EMDB: EMD-16339, EMD-16340, EMD-16341, EMD-16342, and EMD-16343 for focused refinement maps of cPIC, nucleosome, CAK, TFIIH, and composite map, respectively) and PIC-nucleosome<sup>18W</sup> (accession codes EMDB: EMD-16274 and PDB: 8BVW, and EMDB: EMD-16365, EMD-16366, EMD-16367, EMD-16368, and EMD-16369 for focused refinement maps of cPIC, nucleosome, TFIIH, CAK, and composite map, respectively).
- This paper does not report original code.
- Any additional information required to reanalyze the data reported in this paper is available from the [lead contact](#) upon request.

## METHOD DETAILS

### Nucleosome reconstitution

Adenoviral major late promoter (AdMLP) DNA scaffolds containing a 147 bp Widom-601 sequence, which was located at different distances from the TSS, were inserted into pUC119 vectors ([STAR Methods](#)). DNA templates were amplified by PCR from these vectors and purified through Resource Q 6 ml (GE Healthcare), using a gradient of 0-50% TE high-salt buffer (10 mM Tris pH 8.0, 1 mM EDTA pH 8.0, 2 M NaCl). Eluates were ethanol-precipitated and resuspended in TE buffer (10 mM Tris pH 8.0, 1 mM EDTA pH 8.0).

Histones preparation and nucleosome reconstitution was performed as described.<sup>52,66</sup> Briefly, *X. laevis* histones were purified from *Escherichia coli* (*E. coli*) BL21(DE3)-RIL, assembled into histone octamers using a HiLoad 16/600 Superdex 200 pg (Cytiva) and then used for nucleosome reconstitution with the above-mentioned templates through salt-gradient dialysis (SGD). Before assembling the PIC-nucleosome complexes, these nucleosomes were further purified over 4% polyacrylamide gels (0.2x TBE) using a Model 491 PrepCell (Bio-Rad), and subsequently dialysed into PIC-buffer (20 mM HEPES pH 7.5, 100 mM KCl, 2.5% glycerol, 2 mM MgCl<sub>2</sub>, 1 mM TCEP) overnight at 4°C. Reconstitutions were checked on 1% agarose gels (0.5x TBE running buffer). Nucleosomes were concentrated on Amicon Millipore 15 ml 50,000 MWCO centrifugal concentrator to a final concentration of 7-9 μM and their concentration was monitored by measuring their absorbance at 260 nm.

### Assembly of mammalian PIC-nucleosome complexes

Human TBP, TFIIA, TFIIIB, TFIIIE, TFIIIF and TFIIH were expressed and purified as described previously.<sup>40,51</sup> Whereas TFIIA and TBP were independently expressed in insect cells, TFIIIB, TFIIIF and TFIIIE were expressed in LOBSTR-BL21(DE3)-RIL *E. coli* and BL21-Codon Plus(DE3)-RIL *E. coli* cells, respectively. All these general transcription factors (GTFs) were purified first using GE HisTrap HP (5 ml), subsequently followed by ion exchange and size exclusion chromatography steps.

TFIIH was cloned in two different insect cell expression vectors: XPD, p8, p52, p44, p62, p34 and XPB in one (7-core TFIIH) and the CAK module subunits MAT1, CDK7 and cyclin H together in a second vector. While the first vector contained N-terminal 6xHis-TEV tags on p44 and p62 and a N-terminal 6xHis-MBP-TEV tag on XPD, all subunits of the CAK module were tagged N-terminally with 6xHis-TEV tags. Hi5 cells expressing the 7-core TFIIH were lysed with an EmulsiFlex-C5 cell disruptor (Avestin) supplemented with DNase I in lysis buffer (25 mM KOH-HEPES pH 7.6, 400 mM KCl, 20% glycerol, 5 mM TCEP, 0.284 μg ml<sup>-1</sup> leupeptin, 1.37 μg ml<sup>-1</sup> pepstatin A, 0.17 mg ml<sup>-1</sup> PMSF and 0.33 mg ml<sup>-1</sup> benzamidine). Lysate was loaded on a self-packed XK16/20 column (Cytiva) with 25 ml of amylose resin (New England Biolabs) in buffer A1 (25 mM KOH-HEPES pH 7.6, 400 mM KCl, 10% glycerol and 2 mM DTT) and eluted with buffer B1 (25 mM KOH-HEPES pH 7.6, 400 mM KCl, 10% glycerol, 2 mM DTT and 100 mM maltose) into a GE HiTrap Q HP (5 ml) column, pre-equilibrated with buffer A1. Elution of the anion exchange step was performed from 0-100% buffer HB1 (25 mM KOH-HEPES pH 7.6, 2000 mM KCl, 10% glycerol and 2 mM DTT), flow-through fractions collected, cleaved with 2.5 mg TEV protease for 8 hr at 4°C and loaded into a GE HiTrap Heparin HP (1 ml) column, pre-equilibrated with buffer HA1 (25 mM KOH-HEPES pH 7.6, 300 mM KCl, 10% glycerol and 2 mM DTT). Elution was performed using 0-100% buffer B1, fractions collected and further purified using a Superose 6 Increase 10/300 GL in buffer GF (25 mM KOH-HEPES pH 7.6, 300 mM KCl, 10% glycerol and 3 mM TCEP). Stoichiometric 7-core TFIIH was concentrated with Vivaspin 6 50,000 MWCO (GE Healthcare), flash-frozen in liquid nitrogen and stored at -70°C. The kinase module of TFIIH was purified as described with minor modifications.<sup>67</sup> In brief, Hi5 cells expressing the kinase were lysed with an EmulsiFlex-C5 cell disruptor (Avestin) supplemented with DNase I in lysis buffer (25 mM KOH-HEPES pH 7.6, 400 mM KCl, 15% glycerol, 1 mM MgCl<sub>2</sub>, 10 μM ZnCl<sub>2</sub>, 30 mM imidazole pH 8.0, 3 mM TCEP, 0.284 μg ml<sup>-1</sup> leupeptin, 1.37 μg ml<sup>-1</sup> pepstatin A, 0.17 mg ml<sup>-1</sup> PMSF and 0.33 mg ml<sup>-1</sup> benzamidine). The clarified lysate was loaded onto a GE HisTrap HP (5 ml) column, pre-equilibrated with lysis buffer, subsequently washed with buffer A1 HisTrap (25 mM KOH-HEPES pH 7.6, 100 mM KCl, 10% glycerol, 30 mM imidazole pH 8.0 and 1 mM DTT) and eluted with a linear gradient of 0-100% of buffer B1 HisTrap (25 mM K-HEPES, pH 7.6, 100 mM KCl, 10% glycerol, 500 mM imidazole pH 8.0 and 1 mM DTT) in 12

CV. Peak fractions were pooled, diluted with buffer A1 IEX (25 mM K-HEPES, pH 7.6, 100 mM KCl, 5% glycerol and 1 mM DTT), incubated with 2.5 mg of TEV protease at 4°C for 8 hr and loaded onto a GE HiTrap Q HP (5 ml), pre-equilibrated with buffer A1 IEX. The column was washed with 10 CV of buffer A1 IEX and eluted with a linear gradient 0–30% buffer B1 IEX (25 mM K-HEPES, pH 7.6, 2000 mM KCl, 5% glycerol and 1 mM DTT) for 80 CV, a step elution with 50% buffer B1 IEX for 2 CV and a final step with 100% buffer B1 IEX for 2 CV. Stoichiometric TFIIH kinase trimer was pooled and concentrated using Vivaspin 20 10,000 MWCO (GE Healthcare) and loaded onto a HiLoad 16/600 Superdex 200 pg (Cytiva) which was eluted with buffer GF2 (25 mM K-HEPES, pH 7.6, 100 mM KCl, 5% glycerol and 2 mM TCEP). Stoichiometric fractions were pooled, concentrated with Vivaspin 20 10,000 MWCO (GE Healthcare), flash-frozen in liquid nitrogen and stored at -70°C.

The 12-subunit RNA Pol II was purified endogenously from *Sus scrofa* thymus tissue as previously reported.<sup>50,53,68</sup> In summary, *S. scrofa* thymus tissue was homogenized in a 2 L blender (Waring) for 3 minutes at 4°C. The homogenized tissue was filtered through two layers of Miracloth, mixed with polyethyleneimine (final concentration 0.04%) and stirred for 30 minutes at 4°C. The solution was centrifuged at maximum speed and pellets resuspended in 0.4 M HepR buffer (25 mM Tris-HCl pH 7.9, 400 mM (NH<sub>4</sub>)<sub>2</sub>SO<sub>4</sub>, 1 mM EDTA, 10 μM ZnCl<sub>2</sub>, 10% glycerol, 0.284 μg ml<sup>-1</sup> leupeptin, 1.37 μg ml<sup>-1</sup> pepstatin A, 0.17 mg ml<sup>-1</sup> PMSF and 0.33 mg ml<sup>-1</sup> benzamidine), centrifuged once more and supernatant adjusted to the conductivity of 0.2 M HepR buffer (25 mM Tris-HCl pH 7.9, 200 mM (NH<sub>4</sub>)<sub>2</sub>SO<sub>4</sub>, 1 mM EDTA, 10 μM ZnCl<sub>2</sub>, 10% glycerol, 0.284 μg ml<sup>-1</sup> leupeptin, 1.37 μg ml<sup>-1</sup> pepstatin A, 0.17 mg ml<sup>-1</sup> PMSF and 0.33 mg ml<sup>-1</sup> benzamidine) with 0 M HepR buffer (25 mM Tris-HCl pH 7.9, 1 mM EDTA, 10 μM ZnCl<sub>2</sub>, 10% glycerol, 0.284 μg ml<sup>-1</sup> leupeptin, 1.37 μg ml<sup>-1</sup> pepstatin A, 0.17 mg ml<sup>-1</sup> PMSF and 0.33 mg ml<sup>-1</sup> benzamidine). This lysate was loaded on a 225-ml MacroPrepQ column, pre-equilibrated in 0.2 M HepR buffer, the column was washed with 0.2 M HepR buffer (supplemented with 1 mM DTT) and eluted with 0.4 M HepR buffer (supplemented with 1 mM DTT). Eluates were pooled, precipitated by addition of (NH<sub>4</sub>)<sub>2</sub>SO<sub>4</sub> to 50% saturation, stirred at 4°C for 1 hr, centrifuged and pellets resuspended in 0 M HepR2 buffer (25 mM Tris-HCl pH 7.9, 1 mM EDTA, 10 μM ZnCl<sub>2</sub>, 10% glycerol, 1 mM sodium metabisulfite, 0.25 mM PMSF and 1 mM benzamidine). The conductivity of the solution was adjusted on ice to that of 0.15 M HepR buffer (25 mM Tris-HCl pH 7.9, 150 mM (NH<sub>4</sub>)<sub>2</sub>SO<sub>4</sub>, 1 mM EDTA, 10 μM ZnCl<sub>2</sub>, 10% glycerol, 1 mM sodium metabisulfite, 0.25 mM PMSF and 1 mM benzamidine), loaded at 4°C on a 5-ml gravity flow column of 8WG16 (αRPB1 CTD) antibody-coupled sepharose, pre-equilibrated in 0.15 M HepR buffer. The antibody column was washed with five column volumes of 0.5 M HepR buffer (25 mM Tris-HCl pH 7.9, 500 mM (NH<sub>4</sub>)<sub>2</sub>SO<sub>4</sub>, 1 mM EDTA, 10 μM ZnCl<sub>2</sub>, 10% glycerol, 1 mM sodium metabisulfite, 0.25 mM PMSF and 1 mM benzamidine) at 4°C, and eluted at room temperature with 0.5 M HepR2 buffer (25 mM Tris-HCl pH 7.9, 500 mM (NH<sub>4</sub>)<sub>2</sub>SO<sub>4</sub>, 1 mM EDTA, 10 μM ZnCl<sub>2</sub>, 50% glycerol, 1 mM sodium metabisulfite, 0.25 mM PMSF and 1 mM benzamidine). Eluted fractions were immediately 5-fold diluted with Pol II dilution buffer (25 mM Tris-HCl pH 7.9, 1 mM EDTA, 10 μM ZnCl<sub>2</sub> and 2 mM DTT). Diluted fractions were pooled, centrifuged and the supernatant loaded to a UnoQ1 column (Bio-Rad), pre-equilibrated with 0.1 M HepR buffer (25 mM Tris-HCl pH 7.9, 100 mM (NH<sub>4</sub>)<sub>2</sub>SO<sub>4</sub>, 1 mM EDTA, 10 μM ZnCl<sub>2</sub> and 2 mM DTT), the column washed and eluted with a 20 CV linear gradient 20–100% from 0.1 M HepR buffer to 0.5 M HepR3 buffer (25 mM Tris-HCl pH 7.9, 500 mM (NH<sub>4</sub>)<sub>2</sub>SO<sub>4</sub>, 1 mM EDTA, 10 μM ZnCl<sub>2</sub> and 2 mM DTT). GDOWN1-free RNA Pol II fractions were pooled, concentrated using an Amicon 100,000 MWCO Ultra Centrifugal Filter (Merck Millipore), buffer exchanged with Pol II final buffer (10 mM HEPES pH 7.5, 150 mM NaCl, 10% glycerol, 10 μM ZnCl<sub>2</sub> and 1 mM DTT), flash-frozen in liquid nitrogen and stored at -70 °C.

The PIC-nucleosome complexes were prepared identically for both AdMLP templates (PIC-Nuc<sup>10W</sup> and PIC-Nuc<sup>18W</sup>), following the previously established protocol.<sup>40,69,70</sup> In short, the 7-subunit core TFIIH (480 pmol) was mixed with the 3-subunit kinase module (480 pmol) to reconstitute the complete 10-subunit TFIIH at 25°C for 10 min. At the same time, RNA Pol II (240 pmol) was pre-incubated with TFIIF (1.2 nmol) at 25°C for 10 min. Subsequently, TFIIH was incubated with TFIIE (480 pmol), the KCl concentration was immediately adjusted to 150 mM with 0-salt buffer (20 mM HEPES pH 7.5, 2.5% glycerol, 2 mM MgCl<sub>2</sub>, 1 mM TCEP) and the subcomplex incubated at 25°C for 5 min. In the meantime, the PIC upstream complex was formed by adding TBP (1.2 nmol), TFIIA (2.4 nmol) and TFIIB (1.2 nmol) to the nucleosomal scaffolds (300 pmol) and incubating it at 25°C for 5 min. Afterwards, both the upstream complex and TFIIH-TFIIE were combined with RNA Pol II-TFIIF and sample salt concentration was decreased to 100 mM KCl by adding 0-salt buffer. This reaction was incubated at ~400 rpm, 25°C for 90–120 min. Once the reaction was finished, the sample was centrifuged at 21,130g for 10–15 min and further purified by gradient ultracentrifugation. 30% of the sample was purified in a gradient for analytical purposes, whereas the remaining 70% was purified by GraFix<sup>71</sup> and used for structural studies. The gradient was prepared from 15% to 40% sucrose in a buffer with 20 mM HEPES pH 7.5, 100 mM KCl, 2.5% glycerol, 2 mM MgCl<sub>2</sub>, 1 mM TCEP, via a BioComp Gradient Master 108 (BioComp Instruments). Sample preparations for cryo-EM were complemented with 0.2% glutaraldehyde in the 40% sucrose solution. The ultracentrifugation step was carried out at 175,000g for 16 h at 4°C. Subsequently, the gradient was fractionated in 200 μl aliquots, checked by SDS-PAGE and Coomassie staining (analytical gradient) or Native-PAGE and SYBR Gold and Coomassie staining. GraFix samples were immediately quenched after fractionation with a cocktail of pH-adjusted 10 mM lysine and 40 mM aspartate. The stoichiometric crosslinked PIC-nucleosome complexes were dialysed for 6–7 hr at 4°C into PIC-dialysis buffer (20 mM HEPES pH 7.5, 75 mM KCl, 1% glycerol, 2 mM MgCl<sub>2</sub>, 1 mM TCEP) in Slide-A-Lyzer MINI Dialysis Devices (0.1 ml, 20 kDa MWCO) (Thermo Fisher Scientific) for sucrose removal.

### Cryo-electron microscopy

Both PIC-nucleosome complexes (~130 μl) were incubated on a floating ~3.0 nm continuous carbon support for 7 min, after which the carbon film was attached to a holey carbon grid (Quantifoil R3.5/1, copper, mesh 200), washed with 4 μl of PIC-dialysis buffer and

placed in a Vitrobot Mark IV (FEI/Thermo Fisher Scientific) under 100% humidity at 4°C. Under these conditions, samples were blotted with force 5 for 2 s and plunged frozen into liquid ethane. Optimal samples were identified using a Glacios transmission-electron microscope (Thermo Fisher Scientific) operated at 200 keV and equipped with a Falcon-III direct-electron detector (Thermo Fisher Scientific). Data was then collected using SerialEM 4.0<sup>54</sup> on a Titan Krios G2 transmission-electron microscope (FEI/Thermo Fisher Scientific) operated at 300 keV, with 20 eV slit width of a QuantumLS energy filter (Gatan), and equipped with a K3 summit direct detector. Imaging was performed at a nominal magnification of 81,000x (corresponding to a pixel size of 1.05 Å/pixel), with 3 s exposure in counting mode and a total dose of 41.58 and 50.45 e<sup>-</sup> per Å<sup>2</sup>, over 40 and 50 frames for PIC-Nuc<sup>18W</sup> and PIC-Nuc<sup>10W</sup>, respectively, at a defocus range from 0.5–1.5 μm. A total of 41517 and 36478 micrographs were collected for PIC-nucleosome<sup>18W</sup> and PIC-nucleosome<sup>10W</sup>, respectively.

### Data processing

Motion correction, CTF-estimation, dose-weighting and particle-picking was performed in Warp 1.0.9.<sup>58</sup> Micrographs were filtered by resolution and motion estimation, yielding a total of 39399 and 29668, on which Warp auto-picking resulted in 4,667,603 and 4,606,320 initial particles for PIC-nucleosome<sup>18W</sup> and PIC-nucleosome<sup>10W</sup>, respectively.

For PIC-nucleosome<sup>18W</sup>, 4,667,603 particles were extracted with a binning factor of 4. The data was initially classified in cryo-SPARC 3.2.0<sup>55</sup> through 4 rounds of 2D and 3D classification where, for the latter, an *ab initio* model was generated in order to sort out falsely picked particles, ice contamination and aggregated particles. After the initial cleaning of the datasets, all subsequent image processing steps were performed using RELION 3.1.0 (Figure S1).<sup>56,57</sup> 1,725,420 particles containing cPIC were merged and unbinned, after which 2 rounds of CTF refinement, masked 3D refinement and Bayesian polishing on cPIC were done to reconstruct the cPIC at 2.6 Å. From these particles, after a series of signal subtraction, where a spherical mask was initially applied to keep the signal coming between the RNA Pol II stalk and foot, and focused masked 3D focused classifications with or without image alignment, we identified a final set of 147,341 particles which contained the CAK module at 3.3 Å. Subsequently, global 3D classifications with alignment were carried out to keep particles containing both TFIH and the nucleosome. After signal subtracting and classifying these 1,462,564 particles with a spherical mask covering TFIH and the nucleosome, the processing was split in order to yield the highest achievable resolution for both TFIH and nucleosome. Regarding TFIH, signal subtraction and 2 rounds of masked 3D focused classification yielded a reconstruction of TFIH at 4.3 Å (188,832 particles). Masked 3D focused refinements led us to obtain XPD-containing TFIH at 4.7 Å and XPB-containing TFIH at 3.9 Å. In addition, reverting signal subtraction on these particles and performing either a masked or global refinement on cPIC or PIC-Nuc<sup>18W</sup> generated maps at 3.0 Å and 4.0 Å, respectively. On the other hand, this same type of classification procedure was employed in order to identify those particles of highest resolution for the nucleosome in 3 subsequent rounds. 246,363 particles containing the nucleosome were then refined to 3.6 Å.

Data processing for PIC-nucleosome<sup>10W</sup> was performed similarly to PIC-nucleosome<sup>18W</sup> (Figure S4). Briefly, after initial cleaning of data, and performing 2 rounds of CTF refinement, masked 3D refinement and Bayesian polishing, we obtained 1,415,094 particles containing cPIC at 2.4 Å. The CAK module could be resolved at 3.8 Å by following a strategy similar as described above for PIC-Nuc<sup>18W</sup>. Secondly, a global 3D classification with alignment was carried out to sort particles that did not contain TFIH (cPIC-Nuc) from the ones that did (PIC-Nuc and PIC-like). The 705,995 particles containing TFIH or TFIH and nucleosome were exhaustively 3D classified, yielding a set of 376,063 particles, whereas the cPIC-Nuc reconstruction was generated from 668,443 particles. For these sets of particles, the cPIC signal was subtracted by applying a spherical mask on the TFIH-Nuc region, subsequently performing a masked 3D focused classification. In the cPIC-Nuc scheme, sorting was aimed at keeping particles with highest resolution details for the nucleosome, whereas for PIC-Nuc we classified for those having the highest occupancy for TFIH-Nuc. A last round of masked 3D focused classification without alignment was performed on both schemes and the TFIH and the nucleosome of highest resolution were selected for further processing. Lastly, signal subtraction was reverted on the final set of particles for both reconstructions, and masked global 3D refinement was applied on cPIC-Nuc<sup>10W</sup> (3.8 Å) and PIC-Nuc<sup>10W</sup> (4.1 Å). For the former, the focused maps of cPIC and the nucleosome were reconstructed at 3.1 Å and 3.2 Å, respectively. As for PIC-Nuc<sup>10W</sup>, focused maps of cPIC, TFIH and the nucleosome were obtained at 3.2 Å, 4.5 Å and 3.5 Å.

The resolution of the reconstructions was determined following the gold-standard Fourier shell correlation (cut-off at 0.143). Sharpening of maps was performed with the postprocessing tool of RELION 3.1.0, which automatically calculated the reported *B*-factors (Table S1). Local resolution was estimated in RELION 3.1.0 using the previously calculated *B*-factors. For the overall and cPIC maps, however, local resolution maps with *B*-factor of 0 Å were determined in RELION 3.1.0 and subsequently used in PHENIX 1.19.2<sup>59</sup> for map-sharpening. Density map figures were made in UCSF ChimeraX-1.4.<sup>62</sup>

### Model building and refinement

Previously built and published structural models (PDB: 7NVS, 6NMI, 7NVW, 7OHC, 6XBZ, 7EGB, 7ZSB)<sup>28,40,43,46,72,73</sup> were rigid-body fitted into the cryo-EM density maps obtained with highest resolution using UCSF Chimera.<sup>61</sup> Iterative rounds of real-space refinement and manual adjustments were performed using ISOLDE 1.3<sup>63</sup> and PHENIX 1.19.2,<sup>59</sup> whereas *de novo* building was performed in COOT 0.9.6.<sup>64</sup> Merging of the refined structural models was done in COOT 0.9.6,<sup>64</sup> and ISOLDE 1.3<sup>63</sup> was used to flexibly fit the linker DNA between cPIC and the nucleosome. Validation statistics from Molprobit<sup>74</sup> showed good geometry and stereochemistry for the final refined models (Table S1). Atomic model figures were made in PyMOL 2.5.0<sup>60</sup> and UCSF ChimeraX-1.4,<sup>62</sup> where the color assigned for every component is consistent throughout the manuscript.

### **In vitro transcription assay**

Transcription initiation assays were performed *in vitro* with reconstituted components as described previously,<sup>40</sup> albeit with minor modifications. DNA templates and nucleosomes were prepared as generated for cryo-EM studies (STAR Methods). DNA was stored at -20°C in TE buffer and nucleosomes were used right after reconstitution.

Briefly, we assembled the PIC step-wise at 25°C on both nucleosome free- and nucleosome-reconstituted DNA templates, as described above. Per reaction replicate, 3.7 pmol of DNA or nucleosome, 4.6 pmol RNA Pol II, 23 pmol TFIIF and TFIIA, 6.9 pmol TFIIE, TFIIH and CAK, 11.5 pmol TBP and TFIIIB were used. Replicates were performed in a final volume of 23.8  $\mu$ l, with final buffer conditions of 3 mM HEPES pH 7.9, 20 mM Tris-HCl pH 7.9, 60 mM KCl, 8 mM MgCl<sub>2</sub>, 2% (w/v) PVA, 3% glycerol, 0.5 mM DTT, 0.5 mg/ml BSA and 20 units RNase inhibitor. After assembling the PIC for 30 min, 1.25  $\mu$ l of 10 mM NTP solution (Thermo Fisher Scientific) was added to each reaction (final concentration 0.5 mM/NTP) and incubated at 30°C for 60 min. Transcription reactions were stopped with 116  $\mu$ l Stop buffer (10 mM Tris-HCl pH 7.5, 300 mM NaCl, 0.5 mM EDTA, 1% SDS and 4  $\mu$ g proteinase K (New England Biolabs)) and incubated for 30-60 minutes at 37°C. Nucleic acids were then precipitated with isopropanol, in presence of 300 mM sodium acetate and 0.5 mg/ml GlycoBlue (Thermo Fisher Scientific), on ice for 60 minutes. After resuspending nucleic acids, they were immediately supplemented with 1 unit DNase I (New England Biolabs) and incubated at 37°C for 60 min to digest the DNA template. A second nucleic acid isolation was performed by precipitating with isopropanol overnight at -20°C. Samples were then resuspended in 10  $\mu$ l of water. RNA samples were diluted with 2x RNA Loading Dye (New England Biolabs), loaded into urea gels (2 M urea, 1x TBE, 6% acrylamide:bis-acrylamide 19:1) and separated by electrophoresis in 1x TBE buffer running buffer for 33 minutes at 180 V. Low Range ssRNA Ladder (New England Biolabs) was used for size reference, gels were stained for 10 min with SYBR<sup>TM</sup> Gold (Invitrogen) and RNA was visualized with a Typhoon 9500 FLA imager (GE Healthcare Life Sciences).

### **TT-seq and MNase-seq data analysis**

TT-seq labeled and total RNA data (raw and processed) and MNase-seq data (DANPOS3 called nucleosome dyad positions) were taken from T. Velychko et al. (unpublished data). Protein-coding genes (RefSeq GCF\_000001405.39, NM) were split into groups based on their RNA synthesis levels as follows: active genes were defined as the genes that are contained in the major transcript isoform annotation taken from T. Velychko et al., which is based on the total RNA expression data. Active genes were further split deciles q1-q10 based on their RNA synthesis level (TT-seq labeled RNA RPKM). Moreover, active genes were selected to have labeled RNA RPKM  $\geq$  0.01 and inactive (off) genes were defined by having RPKM < 0.01 for both labeled and total RNA samples. This cutoff was determined by plotting densities of replicate-averaged log<sub>2</sub> (TT-seq labeled RNA RPKM) values over all genes and selecting a suitable cutoff in the valley between the two peaks of the bimodal distribution. To determine the correct TSS for each of the inactive genes we selected genes with only one RefSeq annotated isoform. For each gene, the +1 nucleosome dyad position was defined by considering nucleosome dyad position(s) falling within the region from TSS to 200 bp downstream. If two nucleosome dyads overlapped this region, the one closer to the TSS was defined as +1 nucleosome, and if no nucleosome dyad was called in this region, the gene was excluded from further analysis. The final gene sets contained 2680 inactive genes and 9970 active genes (997 per RNA synthesis decile), of which 2261 (off), 892 (q1), 812 (q2), 854 (q3), 837 (q4), 875 (q5), 898 (q6), 903 (q7), 913 (q8), 933 (q9) and 956 (q10) had an annotated +1 nucleosome. TSS to +1 nucleosome edge distances were calculated by subtracting 73 bp from the TSS-to-dyad distances.

### **QUANTIFICATION AND STATISTICAL ANALYSIS**

For *in vivo* data analysis, significance between deciles was determined by calculating *p*-values by two-sided Mann-Whitney U-test.

For the *in vitro* transcription assays, intensity values of gels were quantified using ImageJ 2.1.0,<sup>65</sup> subtracted against the background and normalized to the signal of the corresponding reaction of DNA templates without nucleosomes reconstituted. To facilitate comparisons between different nucleosome distances, signals were scaled to the normalized intensity of Nuc<sup>18W</sup>. Statistical analysis was performed using one-way ANOVA tests with Welch's correction to obtain statistical significance (*p* values). All statistical analysis and diagrams were generated using RStudio or GraphPad Prism 9.1.0.



**Molecular Cell, Volume 83**

**Supplemental information**

**Structural basis of transcription reduction**

**by a promoter-proximal +1 nucleosome**

**Julio Abril-Garrido, Christian Dienemann, Frauke Grabbe, Taras Velychko, Michael Lidschreiber, Haibo Wang, and Patrick Cramer**

Supplemental information

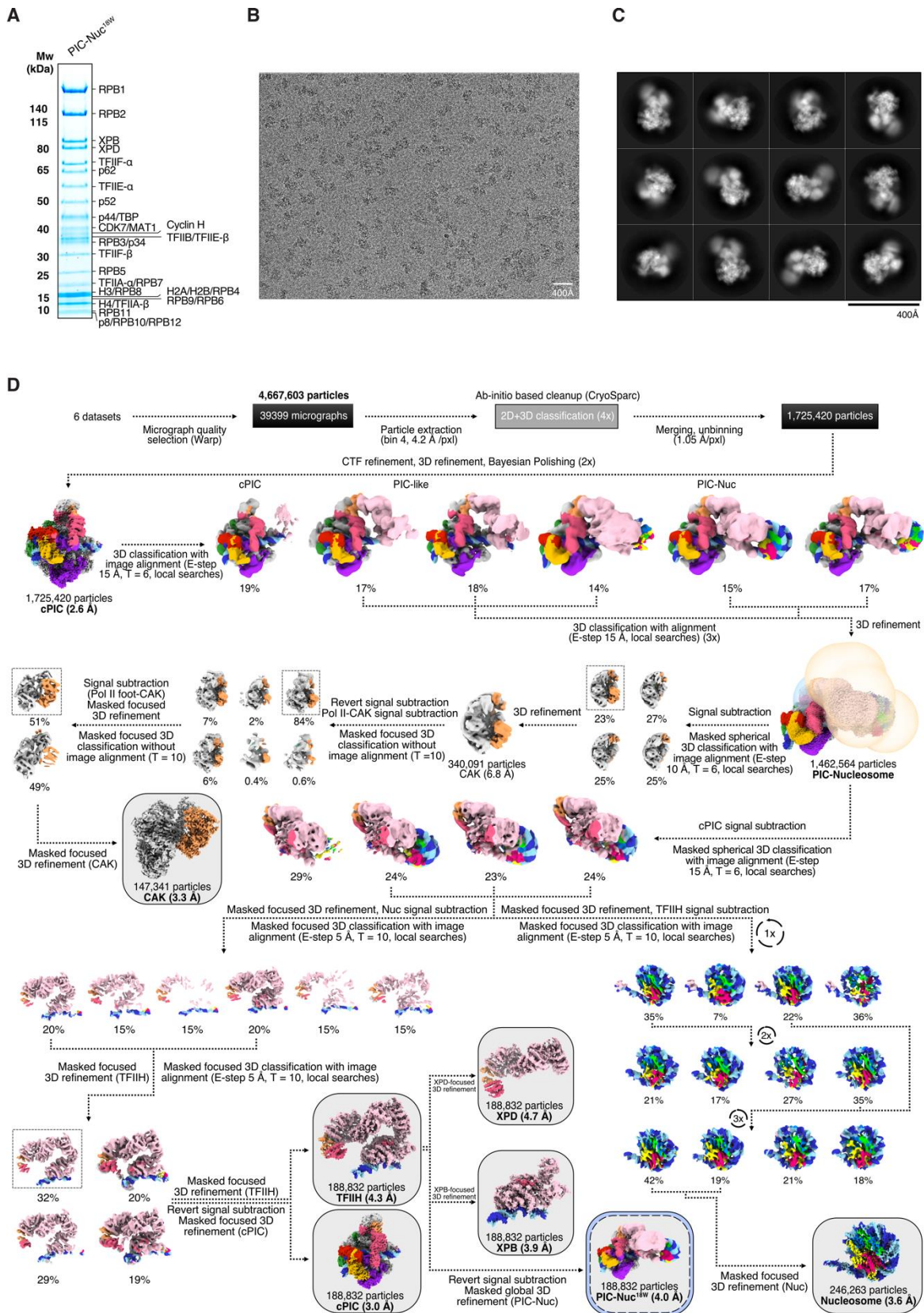


**Figure S1. Sample preparation and cryo-EM processing analysis of PIC-Nucleosome<sup>18W</sup>, Related to Figure 2.**

**(A)** Sucrose gradient fraction used for cryo-EM sample preparation (analyzed by SDS-PAGE). Molecular weight is described on the left side of the gel and assembly components on the right side.

**(B)** Exemplary cryo-EM micrograph. A scale bar is provided at the bottom right of the figure.

**(C)** Representative 2D class averages depicting mammalian PIC-nucleosome<sup>18W</sup>. Scale bar is placed at the bottom right of the figure.

**(D)** Processing classification strategy employed to sort out particles and for structure determination of PIC-Nuc<sup>18W</sup>. Each step of the tree is described on the diagram and the reported resolutions are shown under the respective cryo-EM maps. Final maps used for model building are located within grey boxes, whereas consensus refinements are enclosed in grey-blue boxes.

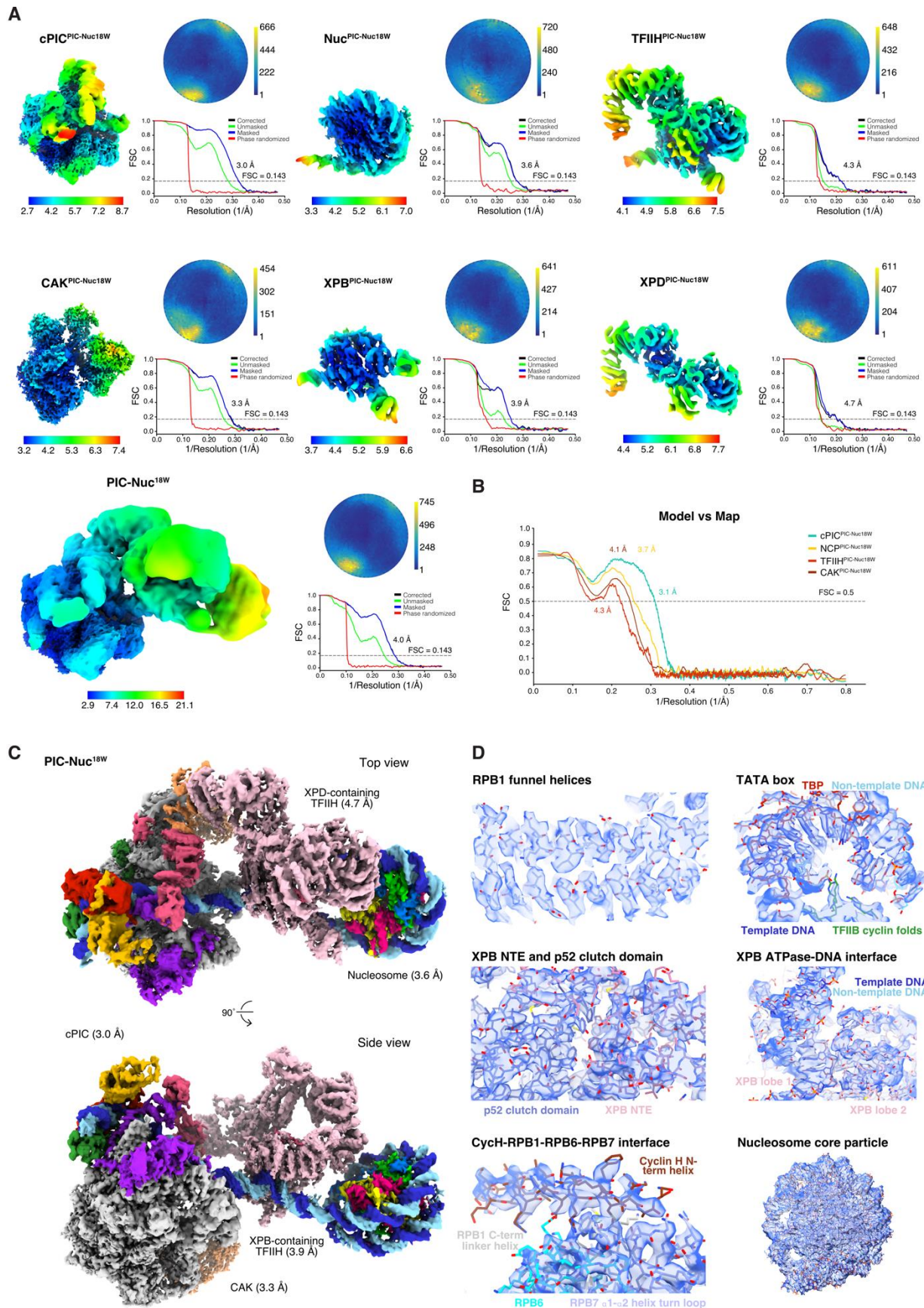


**Figure S2. Map quality assessment of the PIC-nucleosome<sup>18W</sup> structure, Related to Figure 2.**

**(A)** Focused refinements and overall maps filtered and colored by estimated local resolution, shown as top views. The superscript typography of each map is used to differentiate it from the ones shown in **Figure S5**. Their angular distributions and resolution (following the FSC 0.143 cut-off criterion) are provided on the right side of each map.

**(B)** Model-map correlation between the individual focused refined maps, used for model building, and the respective built atomic models. Resolution following the FSC 0.5 cut-off criterion is marked with a dashed line.

**(C)** Composite maps showing individual local refinements in distinct views for PIC-Nuc<sup>18W</sup>. The different protein and DNA components are colored according to the colors used in their structural models, depicted in **Figure 2B**.

**(D)** Cryo-EM density maps (shown in blue surface) fitted to the corresponding region of the modelled structures.



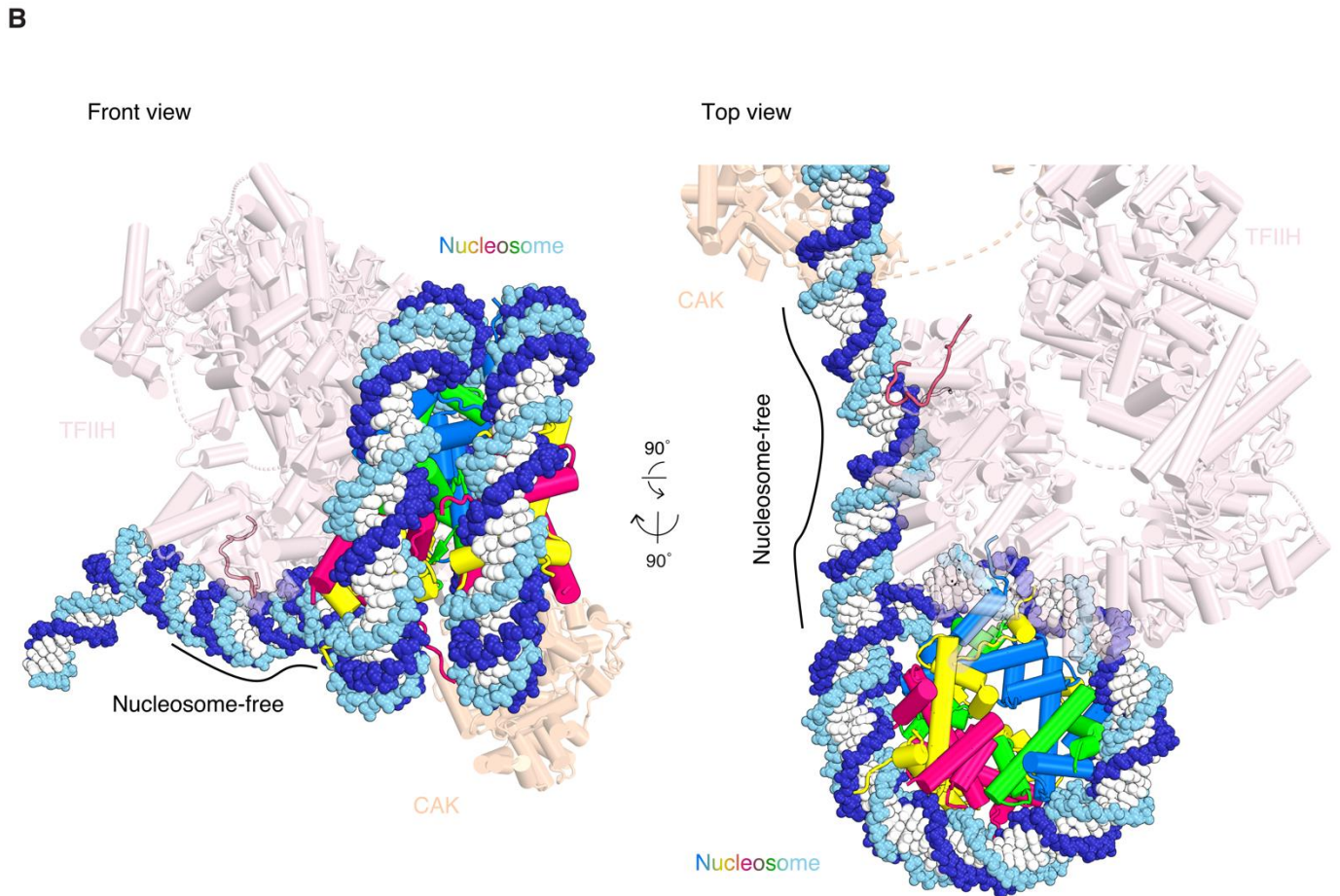
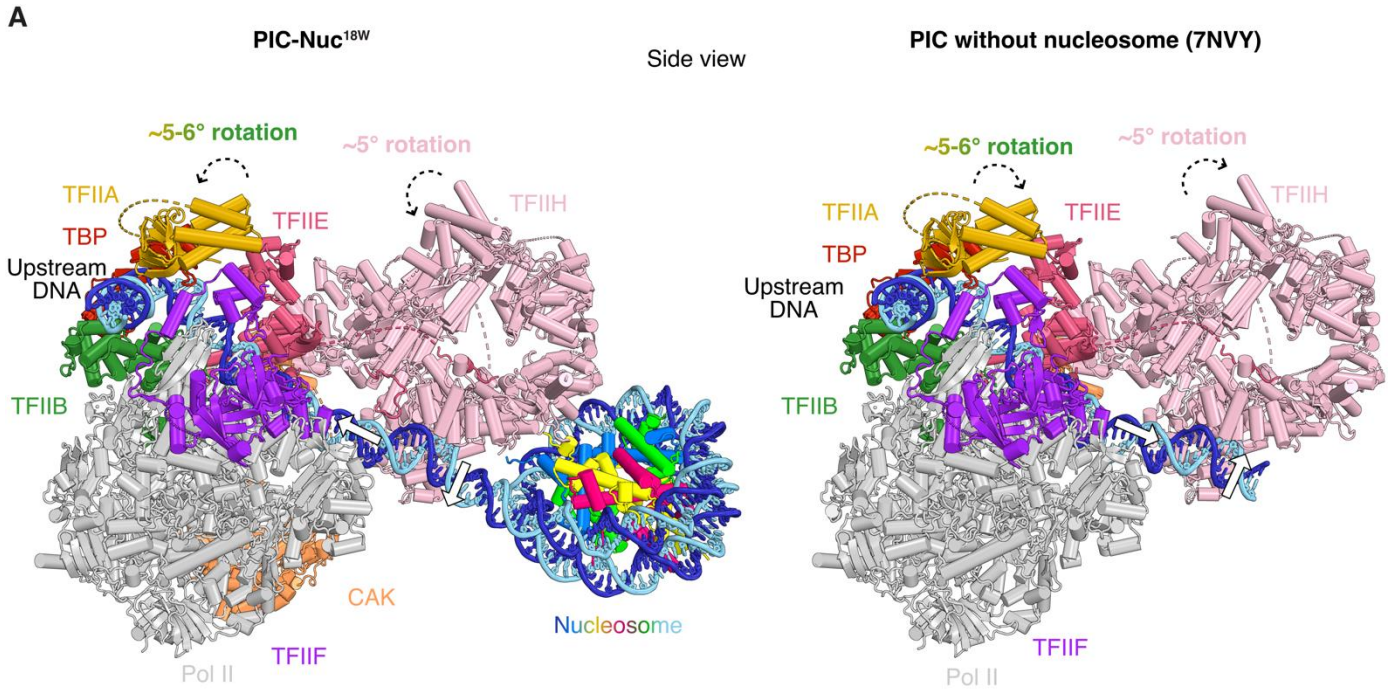




**Figure S3. Downstream DNA is free for TFIID binding in PIC-Nuc<sup>18W</sup> and mammalian PIC without nucleosome, Related to Figure 3.**

**(A)** Comparison of PIC-Nuc<sup>18W</sup> (left panel) with PIC without nucleosome (right panel) (PDB: 7NVY<sup>1</sup>) in side view. PIC is found in its canonical conformation, and only minor movements in the upstream complex were observed. The downstream DNA region is slightly bent when compared to the structure of the nucleosome-free PIC (white arrow). Arrowheads indicate the local motion of different PIC subunits.

**(B)** Front view and top close-up view of TFIID-Nuc<sup>18W</sup>. TFIID binds downstream DNA when the nucleosome is located at a distal position to the promoter region. Nucleosomes are shown in sphere representation and TFIID in transparent cartoon representation. Solid lines denote nucleosome-free DNA.

Superimposition of models was performed by aligning on Pol II. Color of the different components is denoted adjacent to them.

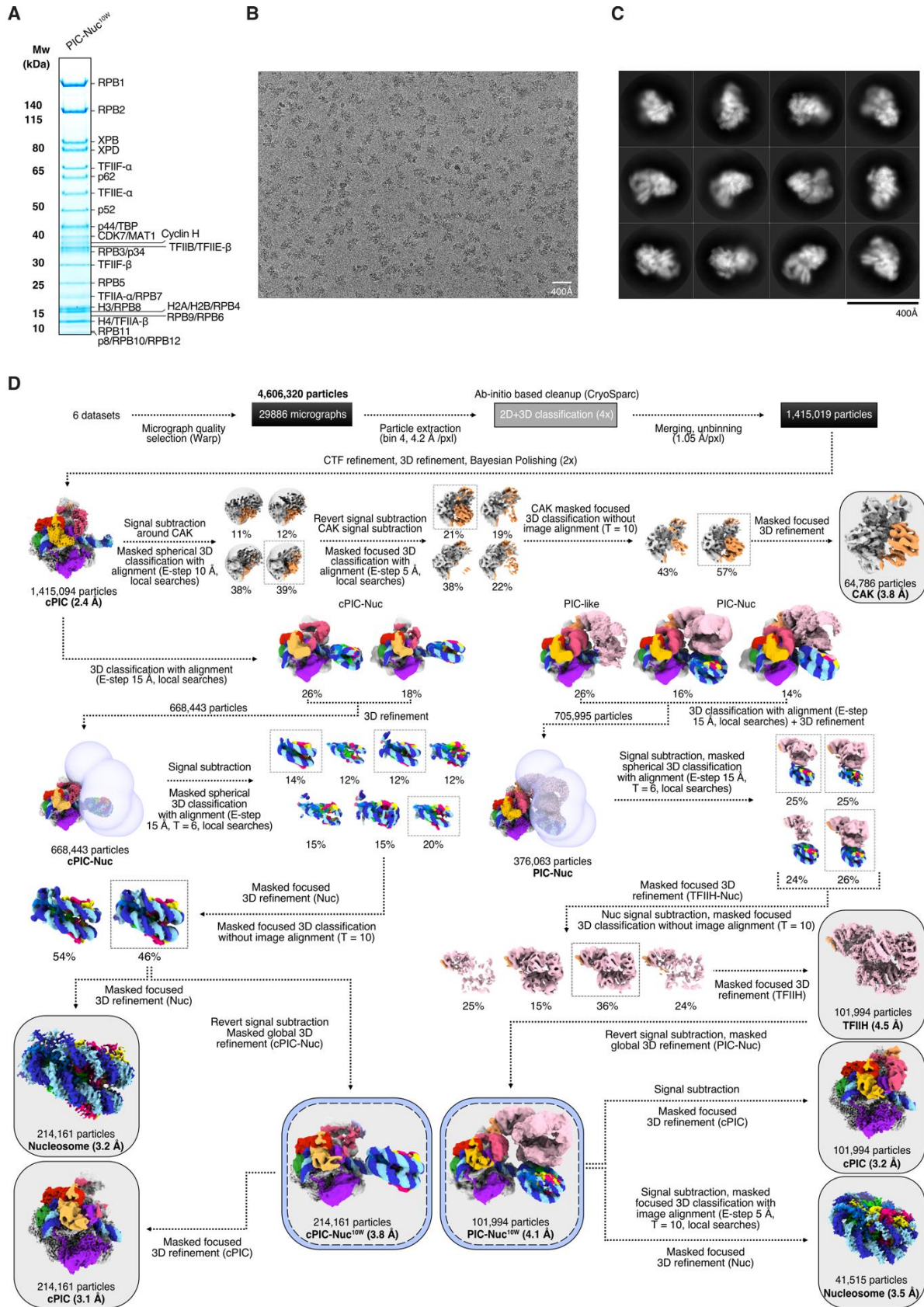


**Figure S4. Sample preparation and cryo-EM processing analysis of PIC-nucleosome<sup>10W</sup>, Related to Figure 2.**

**(A)** Sucrose gradient fraction used for cryo-EM sample preparation (analyzed by SDS-PAGE). Molecular weight is described on the left side of the gel and assembly components on the right side.

**(B)** Exemplary cryo-EM micrograph. A scale bar is provided at the bottom right of the figure.

**(C)** Representative 2D class averages depicting mammalian PIC-nucleosome<sup>10W</sup>. Scale bar is placed at the bottom right of the figure.

**(D)** Processing classification strategy employed to sort out particles and for structure determination of PIC-Nuc<sup>10W</sup>. Each step of the tree is described on the diagram and the reported resolutions are shown under the respective cryo-EM maps. Final maps used for model building are located within grey boxes, whereas consensus refinements are enclosed in grey-blue boxes.



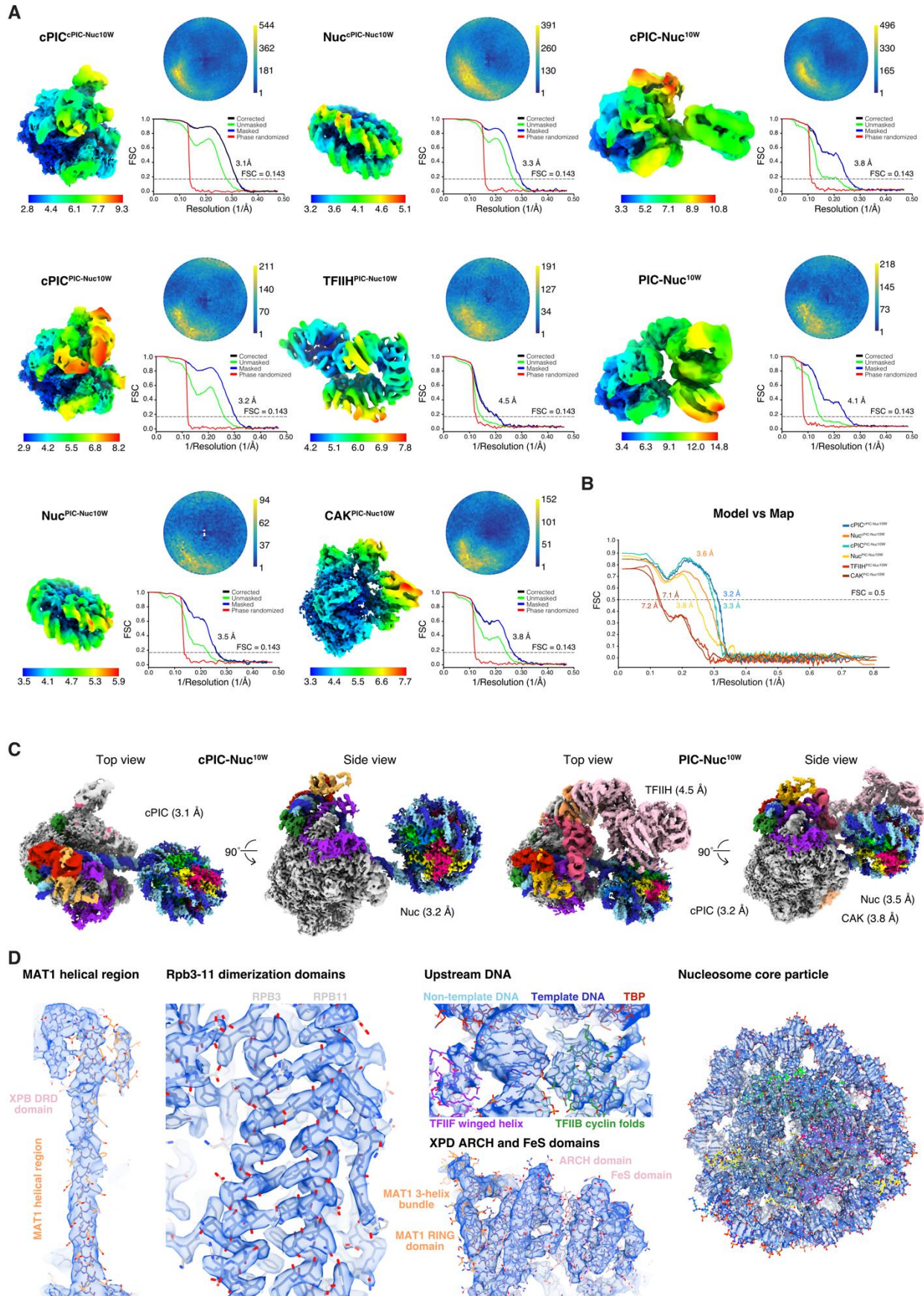
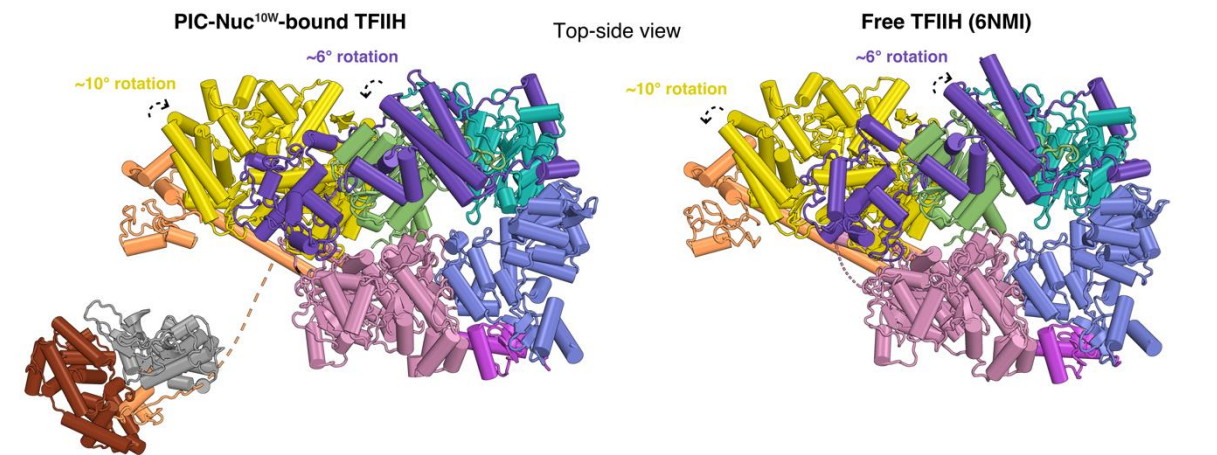
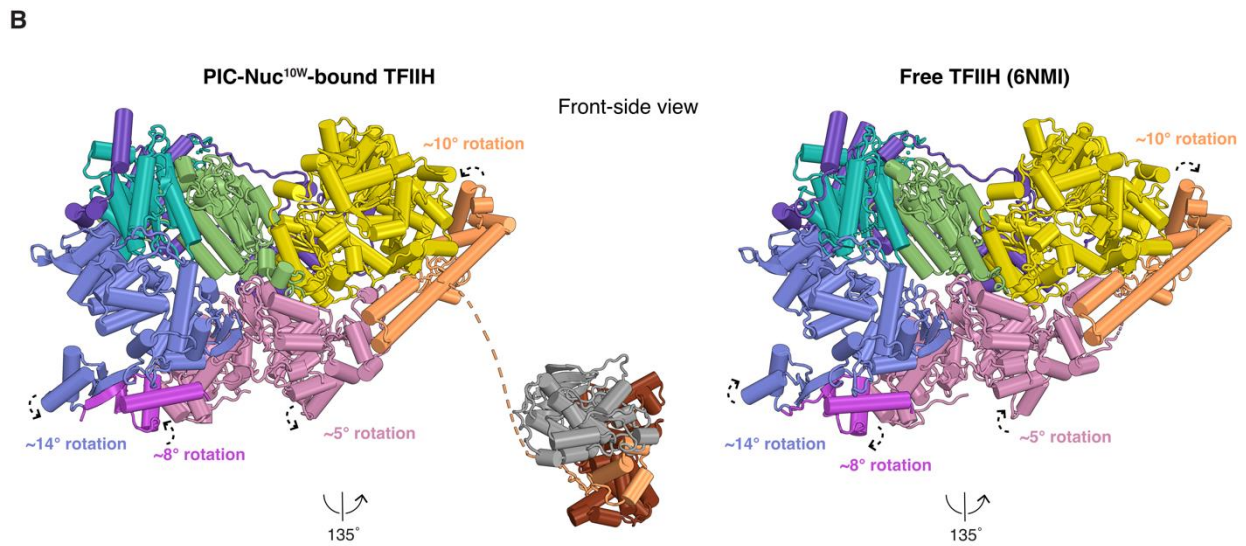
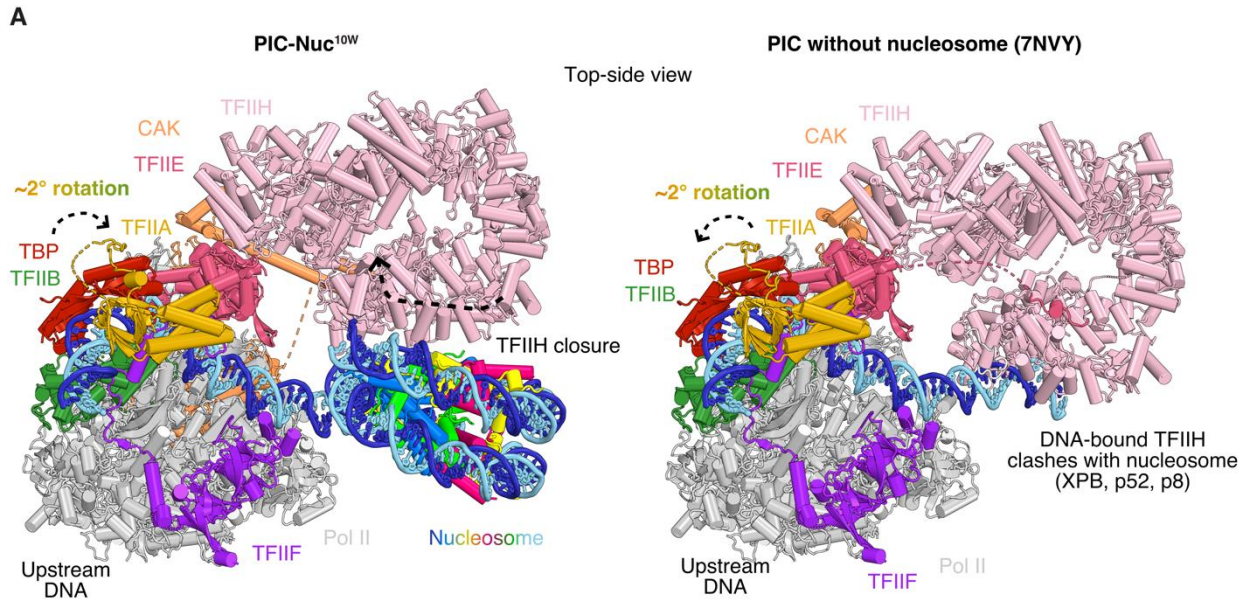


**Figure S5. Map quality assessment of the PIC-nucleosome<sup>10W</sup> structure, Related to Figure 2.**

**(A)** Focused refinements and overall maps filtered and colored by estimated local resolution, shown as top views. The superscript typography of each map indicates whether those particles contained TFIID. Their angular distributions and resolution (following the FSC 0.143 cut-off criterion) are provided on the right side of each map.





■ Non-template 
 ■ Template 
 ■ XPB 
 ■ p52 
 ■ p8 
 ■ p34 
 ■ p62 
 ■ p44 
 ■ XPD 
 ■ MAT1 
 ■ CDK7 
 ■ Cych

**Figure S6. Comparison of PIC-Nuc<sup>10W</sup> and PIC-Nuc<sup>10W</sup>-bound TFIIH with previously reported structures without the nucleosome, Related to Figure 3 and 4.**

**(A)** Comparison of PIC-nucleosome<sup>10W</sup> on a previously reported nucleosome-free PIC structure (PDB: 7NVY<sup>1</sup>) in top-side view. TFIIH now adopts a closed conformation due to the presence of the nucleosome at the region where XPB normally engages free DNA. Arrowheads on TFIIH indicate the closure of TFIIH. Superimposition of the models was performed by aligning on Pol II. Color of the different components is denoted adjacent to them.

**(B)** Comparison of TFIIH from PIC-Nuc<sup>10W</sup> (PIC-Nuc<sup>10W</sup>) (left panel) with free TFIIH (right panel) (PDB: 6NMI<sup>2</sup>) in different views. TFIIH adopts different conformations due to the different position of the nucleosome. Arrowheads indicate the local motion of TFIIH subunits. Superimposition of the models was performed by aligning on TFIIH. TFIIH is depicted in cartoon representation and the color of the different components is denoted exclusively at the bottom legend.



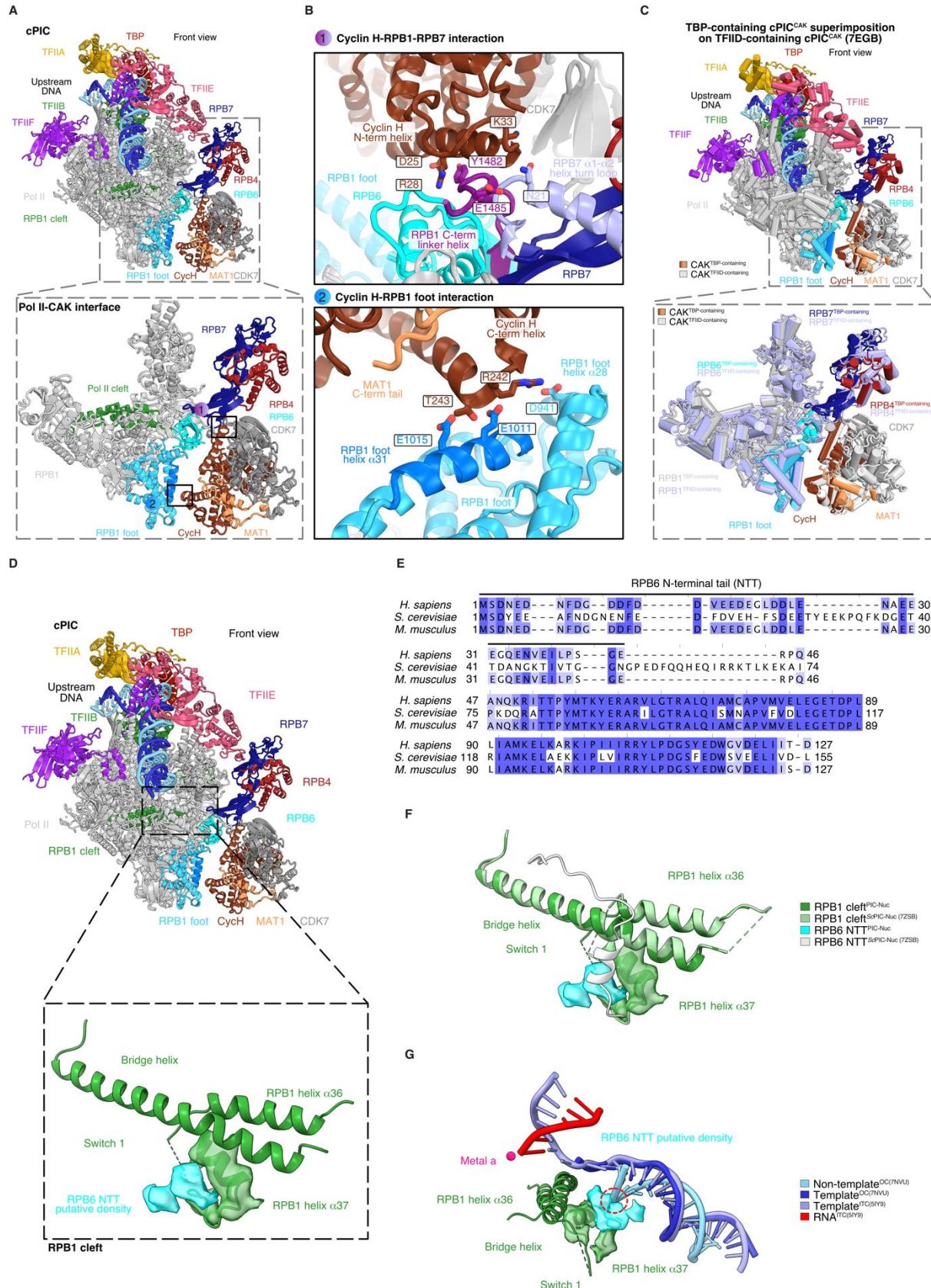


**Figure S7. A PIC-bound nucleosome stabilizes TFIIH CAK and favors ordering of RPB6 NTT, Related to Figure 2.**

**(A)** Enlarged view of the Pol II-CAK interaction interface, shown in front view and within a dashed box. CAK engages via two contact points between the Pol II stalk (RPB4/RPB7) and foot (RPB1) via its subunit Cyclin H. TFIIH and the nucleosome are omitted to facilitate visualization.

**(B)** Cyclin H interacts with Pol II through its N- and C-terminal regions. The N-terminal region contacts electrostatically both RPB1 C-terminus linker helix and RPB7  $\alpha$ 1- $\alpha$ 2 loop, whereas its C-terminus interacts with RPB1 foot helices  $\alpha$ 28 and  $\alpha$ 31. Interacting residues are enclosed in rectangular boxes.

**(C)** Comparison of CAK between TBP-containing (this study) and TFIIID-containing PIC complexes (PDB: 7EGB<sup>3</sup>), shown in front view within a dashed box. There are no perceivable differences between these complexes, except for inherent protein local motion.

**(D)** Magnification of the Pol II cleft, shown in front view and within a dashed box. Putative RPB6 NTT density locates above the helix  $\alpha$ 31 of Pol II cleft. TFIIH and the nucleosome are omitted to facilitate visualization.

**(E)** Protein sequence alignment of RPB6 orthologs in *H. sapiens*, *S. cerevisiae* and *M. musculus*. The alignment was performed with Jalview 2.11.2.4<sup>4</sup> using the T-Coffee algorithm. The RPB6 NTT is denoted with a solid black line. The color code indicates the conservation scoring across different organisms.

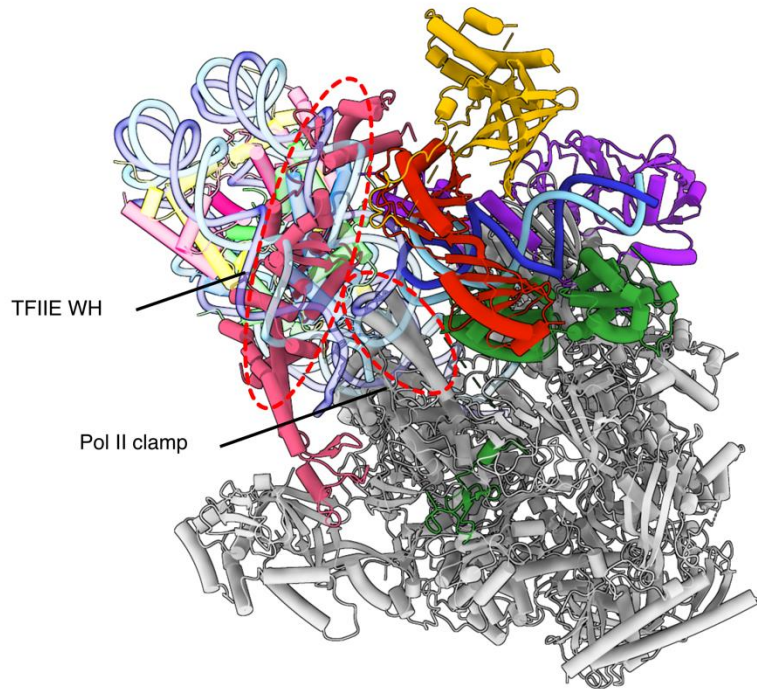
Overlay of the putative RPB6 NTT density of mammalian PIC-nucleosome (this study) on a yeast PIC-nucleosome complex (PDB: 7ZSB<sup>5</sup>) **(F)**, a nucleosome-free mammalian PIC complex with opened promoter DNA (PDB: 7NVU<sup>1</sup>) and a human PIC-initial transcribing complex (ITC, PDB: 5IY9<sup>6</sup>) **(G)**. The putative NTT clashes with the loaded DNA of opened promoter DNA complexes, suggesting the inhibitory function of the nucleosome favors the ordering of such tail.

Colors of the different components in all panels is denoted adjacent to their corresponding subunits and by legends. Superimposition of models shown was performed by aligning on Pol II.

A

**cPIC-Nuc<sup>10W</sup> superimposition on the open promoter complex (7NVU)**

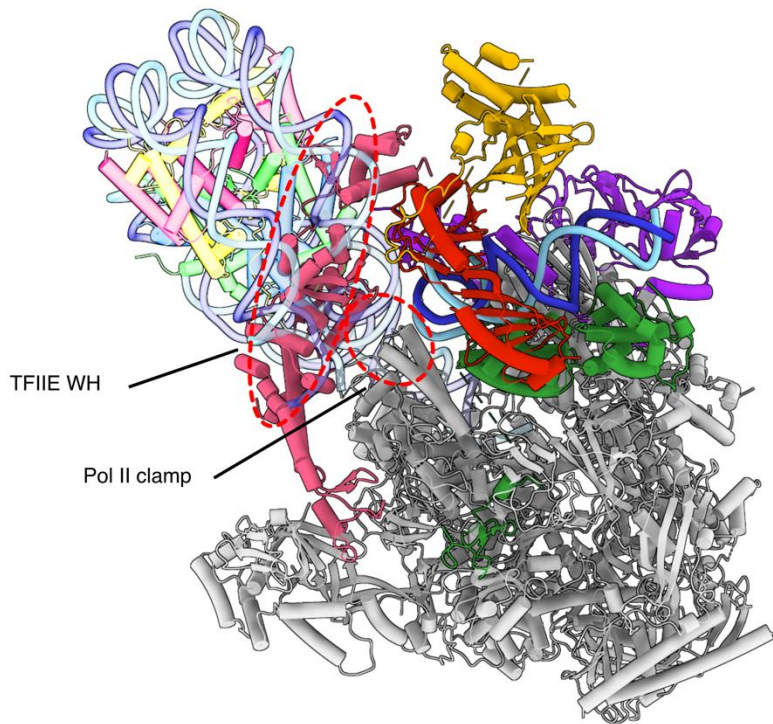
Back-side view



B

**cPIC-Nuc<sup>18W</sup> superimposition on the open promoter complex (7NVU)**

Back-side view



■ Non-template ■ Template ■ TBP ■ TFIIA ■ TFIIB ■ TFIIF ■ TFIIIE ■ H2A ■ H2B ■ H3 ■ H4



**Figure S8. Core PIC-nucleosome complexes are incompatible with DNA opening, Related to Figure 1 and 2.**

**(A) (B)** Modelling of our PIC-nucleosome structures missing TFIID (cPIC) on an open promoter complex (OC, PDB: 7NVU<sup>1</sup>), shown in back-side view. TFIID-independent spontaneous promoter opening would not be compatible on a nucleosomal template since the nucleosome would clash with the Pol II clamp and TFIIE winged helix (WH). Superimposition of the models was performed by aligning on Pol II and the DNA. Steric clashes are indicated with arrowheads and red dashed ovals, proteins are depicted in cartoon representation and the color of the different components is denoted exclusively at the bottom legend.

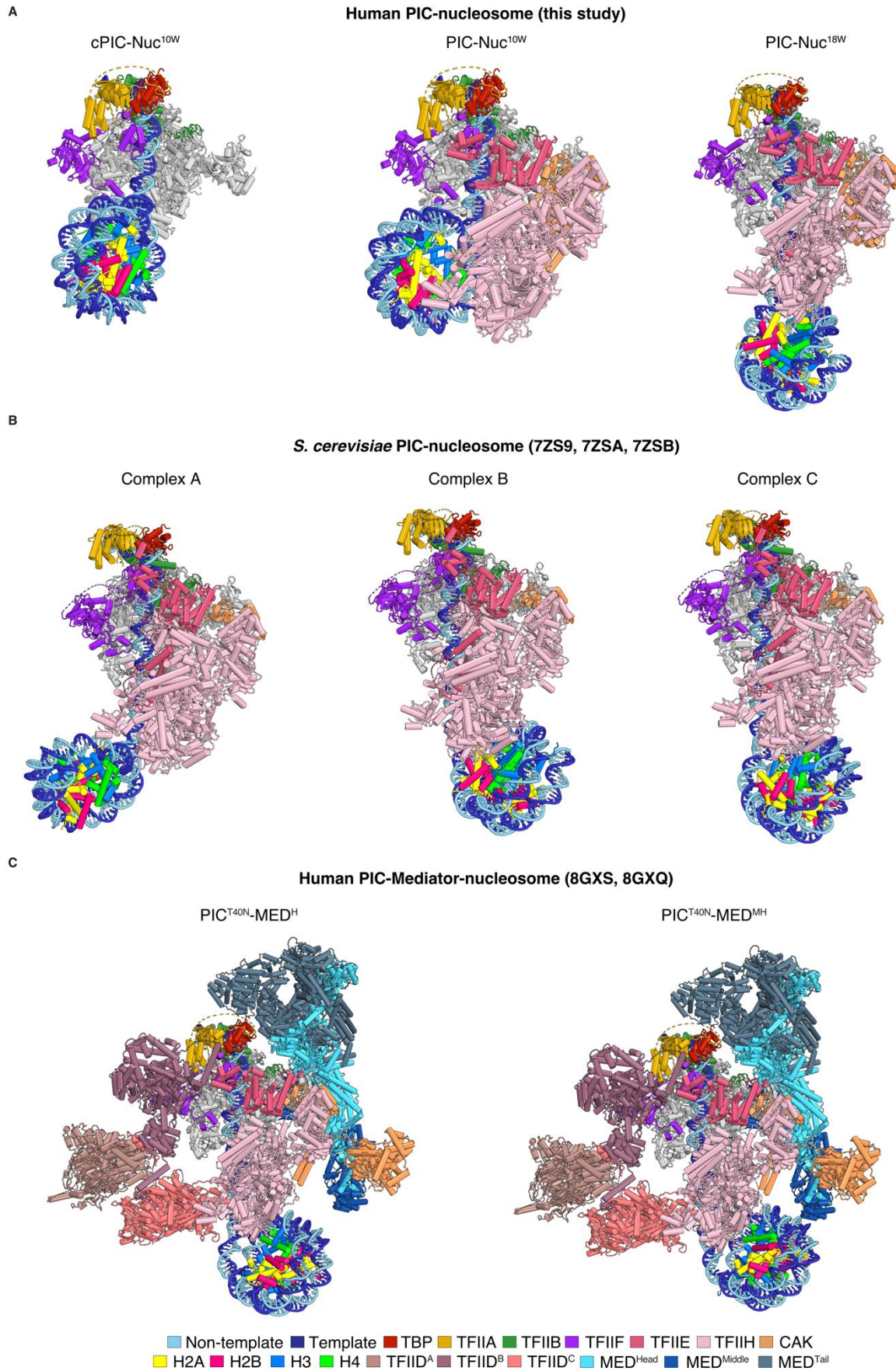


**Figure S9. Comparison of human and yeast PIC-nucleosome complexes, related to Figure 7.**

Models of the PIC-nucleosome complexes determined in **(A)** this study, **(B)** in yeast (PDB: 7ZS9, 7ZSA, 7ZSB<sup>5</sup>) and **(C)** in human (PDB: 8GXS, 8GXQ<sup>7</sup>) Superimposition of the models was performed by aligning on Pol II and the representations shown in the same view. Color of the different components is denoted exclusively at the bottom legend.

**Table S1. Cryo-EM data acquisition, processing and refinement statistics, Related to Figure 2.**

<b>Model name</b>	cPIC-nucleosome <sup>10W</sup>	PIC-nucleosome <sup>10W</sup>	PIC-nucleosome <sup>18W</sup>
PDB code	(PDB: 8BZ1)	(PDB: 8BYQ)	(PDB: 8BVW)
Map code	(EMDB: EMD-16335)	(EMDB: EMD-16331)	(EMDB: EMD-16274)
<b>Data collection and processing</b>			
Magnification	81,000x	81,000x	81,000x
Voltage (kV)	300	300	300
Electron exposure (e-/Å <sup>2</sup> )	50.45	50.45	41.58
Defocus range (µm)	0.6 – 1.3	0.6 – 1.3	0.5 – 1.5
Pixel size (Å)	1.05	1.05	1.05
Initial particle images (no.)	4,606,320	4,606,320	4,667,603
Symmetry imposed	C1	C1	C1
Final particle images (no.)	214,161	101,994	188,832
Map resolution (Å) at FSC = 0-143	3.8	4.1	4.0
Map resolution range (Å)	2.8 – 7.7	2.9 – 8.2	2.7 – 8.7
Map sharpening B factor (Å <sup>2</sup> )	-90	-150	-114
<b>Refinement</b>			
Initial models used (PDB code)	7NVS, 7OHC	7NVS, 7OHC, 6NMI, 6XBZ, 7EGB	7NVS, 7OHC, 7ZSB, 7NVW, 6XBZ, 7EGB
<b>Model composition</b>			
Non-hydrogen atoms	53411	86010	84811
Protein residues	5667	9687	9510
Nucleotides	396	396	412
Ligands	ZN: 9 MG: 1	ZN: 16 MG: 1 SF4: 1 UNK: 154	ZN: 17 MG: 1 SF4: 1 UNK: 27
<b>Mean B factors (Å<sup>2</sup>)</b>			
Protein	117.33	176.57	125.41
Nucleotides	145.93	212.46	212.92
Ligand	146.29	223.85	136.37
<b>R.m.s. deviations</b>			
Bond lengths (Å)	0.004	0.005	0.006
Bond angles (°)	0.737	0.860	0.896
<b>Validation</b>			
MolProbity score	1.22	1.47	1.46
Clashscore	4.46	6.52	5.48
Poor rotamers (%)	0.00	0.06	0.04
<b>Ramachandran plot</b>			
Favored (%)	98.19	97.44	96.93
Allowed (%)	1.81	2.56	3.07
Disallowed (%)	0.00	0.00	0.00

PDB: Protein Data Bank; EMD: Electron Microscopy Data Bank; FSC: Fourier Shell Correlation; R.m.s.: root-mean-square



## Supplemental references

1. Aibara, S., Schilbach, S., and Cramer, P. (2021). Structures of mammalian RNA polymerase II pre-initiation complexes. *Nature* 594, 124-128. 10.1038/s41586-021-03554-8.
2. Greber, B.J., Toso, D.B., Fang, J., and Nogales, E. (2019). The complete structure of the human TFIID core complex. *Elife* 8. 10.7554/eLife.44771.
3. Chen, X., Qi, Y., Wu, Z., Wang, X., Li, J., Zhao, D., Hou, H., Li, Y., Yu, Z., Liu, W., et al. (2021). Structural insights into preinitiation complex assembly on core promoters. *Science* 372. 10.1126/science.aba8490.
4. Waterhouse, A.M., Procter, J.B., Martin, D.M., Clamp, M., and Barton, G.J. (2009). Jalview Version 2--a multiple sequence alignment editor and analysis workbench. *Bioinformatics* 25, 1189-1191. 10.1093/bioinformatics/btp033.
5. Wang, H., Schilbach, S., Ninov, M., Urlaub, H., and Cramer, P. (2022). Structures of transcription preinitiation complex engaged with the +1 nucleosome. *Nat Struct Mol Biol*. 10.1038/s41594-022-00865-w.
6. He, Y., Yan, C., Fang, J., Inouye, C., Tjian, R., Ivanov, I., and Nogales, E. (2016). Near-atomic resolution visualization of human transcription promoter opening. *Nature* 533, 359-365. 10.1038/nature17970.
7. Chen, X., Wang, X., Liu, W., Ren, Y., Qu, X., Li, J., Yin, X., and Xu, Y. (2022). Structures of +1 nucleosome-bound PIC-Mediator complex. *Science* 378, 62-68. 10.1126/science.abn8131.